Check for updates

Received: 29 August 2022 | Revised: 24 May 2023 | Accepted: 2 June 2023 | Published on: 24 July 2023

DOI: 10.1002/qj.4505

Quarterly Journal of the Royal Meteorological Society RMetS

RESEARCH ARTICLE

Statistical relevance of meteorological ambient conditions and cell attributes for nowcasting the life cycle of convective storms

Jannik Wilhelm[1] | **Kathrin Wapler**[2] | **Ulrich Blahak**[2] | **Roland Potthast**[2,3] | **Michael Kunz**[1,4]

[1]Institute of Meteorology and Climate Research (IMK-TRO), Karlsruhe Institute of Technology, Karlsruhe, Germany

[2]German Weather Service, Offenbach, Germany

[3]Department of Mathematics and Statistics, University of Reading, Reading, UK

[4]Center for Disaster Management and Risk Reduction Technology, Karlsruhe Institute of Technology, Karlsruhe, Germany

Correspondence
J. Wilhelm, Institute of Meteorology and Climate Research (IMK-TRO), Karlsruhe Institute of Technology (KIT), Karlsruhe, Germany.
Email: jannik.wilhelm@kit.edu

Funding information
Bundesministerium für Digitales und Verkehr, Grant/Award Number: Z30/SeV/288.3/1582/LF16

Abstract

The usually short lifetime of convective storms and their rapid development during unstable weather conditions makes forecasting these storms challenging. It is necessary, therefore, to improve the procedures for estimating the storms' expected life cycles, including the storms' lifetime, size, and intensity development. We present an analysis of the life cycles of convective cells in Germany, focusing on the relevance of the prevailing atmospheric conditions. Using data from the radar-based cell detection and tracking algorithm KONRAD of the German Weather Service, the life cycles of isolated convective storms are analysed for the summer half-years from 2011 to 2016. In addition, numerous convection-relevant atmospheric ambient variables (e.g., deep-layer shear, convective available potential energy, lifted index), which were calculated using high-resolution COSMO-EU assimilation analyses (0.0625°), are combined with the life cycles. The statistical analyses of the life cycles reveal that rapid initial area growth supports wider horizontal expansion of a cell in the subsequent development and, indirectly, a longer lifetime. Specifically, the information about the initial horizontal cell area is the most important predictor for the lifetime and expected maximum cell area during the life cycle. However, its predictive skill turns out to be moderate at most, but still considerably higher than the skill of any ambient variable is. Of the latter, measures of midtropospheric mean wind and vertical wind shear are most suitable for distinguishing between convective cells with short lifetime and those with long lifetime. Higher thermal instability is associated with faster initial growth, thus favouring larger and longer living cells. A detailed objective correlation analysis between ambient variables, coupled with analyses discriminating groups of different lifetime and maximum cell area, makes it possible to gain new insights into their statistical connections. The results of this study provide guidance for predictor selection and advancements of nowcasting applications.

KEYWORDS

convective storms, life cycle, multisource data, nowcasting, statistics, weather prediction

This is an open access article under the terms of the Creative Commons Attribution License, which permits use, distribution and reproduction in any medium, provided the original work is properly cited.
© 2023 The Authors. *Quarterly Journal of the Royal Meteorological Society* published by John Wiley & Sons Ltd on behalf of the Royal Meteorological Society.

1 | INTRODUCTION

Forecasting and nowcasting convective storms are challenging tasks for weather services. Every year, these storms cause substantial damage to infrastructure, property, and agricultural areas. In central Europe, convective storms occur most frequently from April to September, leading to damage totalling billions of euros, as well as many injuries and fatalities every year (Púčik *et al.,* 2019; Taszarek *et al.,* 2019). In Germany alone, some single convective events during the past decade caused more than €100 million to occasionally more than €1 billion in damage by, for instance, local flash floods stemming from long-living quasi-stationary cells or by extended hail swaths containing large hailstones produced by long-living supercells (e.g., Piper *et al.,* 2016; Bronstert *et al.,* 2017; Hübl, 2017; Vogel *et al.,* 2017; Kunz *et al.,* 2018; Mohr *et al.,* 2020; Wilhelm *et al.,* 2021). Difficulties in forecasting convective storms arise from the complex processes and scale interactions involved, the lack of comprehensive and detailed observational information, and the limited representation of deep moist convection (DMC) in numerical weather prediction (NWP) models. Improvements in estimating the short-term evolution of convective storms are essential for providing temporally and spatially more accurate warnings to the public and emergency services (e.g., Wapler *et al.,* 2018).

During the past few decades, numerous dynamical quantities and so-called convective indices quantifying different atmospheric prerequisites for the development of convective storms (thermal instability, sufficient moisture, lifting; see Doswell, 1987; Johns and Doswell, 1992) have been invented. This has allowed for the ingredients-based forecasting of storm occurrences and associated hazards (e.g., Huntrieser *et al.,* 1997; Rasmussen and Blanchard, 1998; Haklander and van Delden, 2003; Manzato, 2003; Brooks, 2007; Kunz, 2007). Relationships between thunderstorm occurrences or different convective phenomena and ambient conditions have recently been analysed in several studies using radar, satellite, lightning, radiosonde, and model data, unravelling characteristic connections in a statistical sense (e.g., Kunz, 2007; Brooks, 2009; Kaltenböck *et al.,* 2009; Mohr and Kunz, 2013; Púčik *et al.,* 2015; Ukkonen *et al.,* 2017; Westermayer *et al.,* 2017; Kunz *et al.,* 2020; Taszarek *et al.,* 2021). An insufficiently clarified question is whether and which of the ambient variables and parameters have the highest prediction skill for the life-cycle properties of convective cells, such as lifetime, the development of the cells' extent in terms of regions of high radar reflectivity and precipitation, and the development of the cells' intensity characterised, for example, by a large fraction of very high radar reflectivity. Incorporating information from these ambient variables about the expected life cycles might help with reducing the intricacies of operational nowcasting procedures.

Zöbisch *et al.* (2020) recently presented a study on the characteristics of DMC aimed at improving thunderstorm nowcasting. Specifically, they provided a detailed review of studies investigating convective storm life cycles during the past few decades. As (severe) thunderstorms occur in many regions of the Earth, on a broad range of scales, and under a large variety of atmospheric conditions, drawing generally valid conclusions from life-cycle studies is a challenging task. Nevertheless, improved forecasting and nowcasting techniques through improved life-cycle representation have the potential to lead to more reliable warnings, and thus save lives and prevent damage.

Ordinary and widely used nowcasting techniques for hazards related to convective storms involve predicting their development for the next minutes to hours. These methods mainly extrapolate the track of a storm that a certain tracking algorithm has detected based on temporally highly resolved radar or satellite observations (Wang *et al.,* 2017). Possible changes in intensity, size, propagation speed, and direction, however, usually are not taken into account with these techniques. Still, convective cells are intrinsically in a state of alteration during their life cycles (e.g., Markowski and Richardson, 2010). One of the challenges of thunderstorm nowcasting "is the improvement of predictions of the remaining lifetime of existing thunderstorms […] regardless of their organisation type" (or life-cycle phase; Zöbisch *et al.,* 2020). The organisation type, or convective mode, however, depends on the mesoscale atmospheric ambient conditions that may be described by meteorological parameters such as the mean wind and the vertical wind shear in the lower to middle troposphere (e.g., Weisman and Klemp, 1982; Markowski and Richardson, 2010; Trapp, 2013).

Some nowcasting methods already use information about ambient conditions from the NWP model data along with observational data: German Weather Service's (DWD's) nowcasting system, NowCastMix, is used for nowcasting both summer and winter warning events (James *et al.,* 2018). NowCastMix combines NWP forecasts, real-time weather station reports, lightning data, weather radar products, and data from convective cell detection and tracking methods with a fuzzy logic approach to produce an objective hazard warning. The ProbSevere system of the National Oceanic and Atmospheric Administration extracts and integrates data from rapid-update NWP forecasts, satellite, lightning, and radar data via multiplatform multiscale storm identification and tracking. This is done to compute severe hazard probabilities in a statistical framework using naive Bayesian classifiers for machine learning (Cintineo *et al.,* 2020).

1477870x, 2023, 755, Downloaded from https://rmets.onlinelibrary.wiley.com/doi/10.1002/qj.4505 by Karlsruher Institution F. Technologie, Wiley Online Library on [10/11/2023]. See the Terms and Conditions (https://onlinelibrary.wiley.com/terms-and-conditions) on Wiley Online Library for rules of use; OA articles are governed by the applicable Creative Commons License

The Context and Scale Oriented Thunderstorm Satellite Predictors Development (COALITION-3) system of the Swiss weather service, MeteoSwiss, probabilistically estimates storm developments for the next hour on the basis of NWP, satellite, lightning, and radar data. It also takes into account the influence of orography and uses gradient-boosted decision trees for machine learning (Nisi *et al.,* 2014; Hamann *et al.,* 2019). For nowcasting lead times of 15 min and more, they found that NWP model information becomes the most important source. Recently, Mecikalski *et al.* (2021) presented a multisensor (satellite, lightning, and radar data) random forest approach to assess predictors' importance and the predictive skill of severe thunderstorm and tornado warnings in a multivariate framework. Because they suspected that "a severe storm adjacent to a nonsevere storm could be assigned the same NWP fields in terms of kinematic and thermodynamic fields", they did not consider the ambient conditions of the storms.

For overcoming the simple extrapolation of thunderstorm tracks and inspecting the importance of ambient variables in detail, it is imperative to investigate which ambient variables are strong predictors for a sound life-cycle estimation, which may enhance today's nowcasting systems. Moreover, insights into the importance of the parameters compared with information about the cells' histories at different life-cycle stages are essential. These questions are addressed in the study at hand, where the main element is the statistical analysis of the relationships between life-cycle attributes and ambient variables. In particular, following the investigations of Wilhelm (2022), this article addresses the following two main scientific questions:

(1) Under which range of prevailing ambient conditions does DMC develop, and how are the related ambient variables statistically correlated with each other and with cell attributes at the beginning of the cells' life cycles?
(2) Which ambient variables and cell attributes correlate best with the storm properties of lifetime and maximum area, indicating the potential for the improvement of nowcasting procedures?

Section 2 introduces KONRAD (from the German Konvektionsentwicklung in Radarprodukten, meaning convection evolution in radar products; Lang, 2001) cell detection and tracking data, as well as Consortium for Small-scale Modelling (COSMO-EU) assimilation analyses, and it describes the methodology of the combination of object data (radar) and meteorological fields (model). Section 3 briefly discusses the convective cell properties, provides an overview of the ambient conditions prevailing during the storms detected, and quantifies the statistical correlations between them. In Section 4, the correlation of ambient variables, initial cell growth, and life-cycle characteristics (like cell lifetime and maximum cell area) is quantified, thus highlighting their potential predictive value. Section 5 summarises and discusses the most important findings.

2 | DATA AND METHODS

The analyses presented in this study are based on two datasets. First, the life cycles of convective cells are represented by data of DWD's operational radar-based cell detection and tracking algorithm, KONRAD. Second, meteorological ambient conditions are assessed by means of assimilation analyses of DWD's formerly operational regional NWP model, COSMO-EU. The investigation period ranges from 2011 to 2016, with only the summer half-years being considered (April to September). These 6 months mark the time span when most thunderstorms occur in Germany (e.g., Wapler and James, 2015). Both tracking and model data, their preparation, and their combination are described separately in the following.

2.1 | Observation data: Convective cell detection and tracking with KONRAD

As described in detail in Wapler (2021), the cell detection and tracking algorithm KONRAD utilises two-dimensional (2D) composite radar reflectivity data from the terrain-following near-surface precipitation scan (RX composite) of the German C-band weather radar network consisting of 17 operational radar stations (Mammen *et al.,* 2010). The time and horizontal resolution of the 2D composite are 5 min and 1 km respectively. Thus, KONRAD runs operationally every 5 min, defining a convective cell numerically as a continuous area of at least 15 km^2 size with a radar reflectivity factor Z of 46 dBZ or more (cell area). This operationally used threshold is relatively high compared with other algorithms and studies (e.g., Goudenhoofdt and Delobbe, 2013; Nisi *et al.,* 2018, and references therein), so considerable parts of the cells' cumulus and dissipation stages are not included. The tracking of convective cells is realised by matching the cells of two consecutive radar composites as described in Lang *et al.* (2003). Similar to many cell detection and tracking algorithms, KONRAD is not able to correctly handle all cell life cycles, especially when it comes to splitting or merging two or more cells. Owing to the strict numerical definition of a cell as already mentioned herein, many splits or merges seen via KONRAD do not represent real

1477870x, 2023, 755, Downloaded from https://rmets.onlinelibrary.wiley.com/doi/10.1002/qj.4505 by Karlsruher Institution F. Technologie, Wiley Online Library on [10/11/2023]. See the Terms and Conditions (https://onlinelibrary.wiley.com/terms-and-conditions) on Wiley Online Library for rules of use; OA articles are governed by the applicable Creative Commons License

physical cell splits or merges. Moreover, obtaining a single full convective cell track is not feasible in cases of multicells, cell clusters, or mesoscale convective systems, which appear frequently.

With this tracking data, the life cycles (i.e., object-based sequences of multiple cell attributes) of the convective cells detected are analysed, and cells that have been detected at only one point in time are discarded. Cell attributes comprise age, size, propagation direction, and speed, as well as the position of the reflectivity-weighted centroid, and the cell-enframing latitude–longitude rectangle (see Section 2.3). For the purpose of avoiding a priori misleading interpretations arising from the difficulties of defining the cell's full life cycle as described herein, a vicinity criterion is applied: all detected cells that might have developed or dissipated close to another one (neighbour) are discarded, as also are their neighbours. A sensitivity study revealed 5 km as a good compromise for the minimum required distance between the latitude–longitude rectangles of two cells so that they are not filtered out based on the vicinity criterion. Thus, the analysis presented in this study focuses primarily on isolated convective storms (i.e., single cells or supercells) that have undisturbed life cycles and that do not dynamically interact with other cells. Hence, the focus on isolated convection is reasonable: on the one hand, supercells exhibit the greatest damage potential (e.g., Kunz *et al.,* 2018; Wilhelm *et al.,* 2021); on the other hand, single cells represent the "most simple cases" and a sufficiently large fraction of the available data (see later). It should be noted, however, that the isolated convection might still have been influenced by weaker cells in the vicinity that did not fulfil the KONRAD criteria. The vicinity filter is connected with more filters that discard cells due to missing life-cycle information in connection with the radar coverage or with unrealistic propagation/evolution tendencies (e.g., direction change of more than 30°/5 min, smoothed over three detection times; growth of more than 50 km^2/5 min). Of the original 103,563 life cycles, 35.5% are discarded based on the vicinity filter, 27.3% are discarded based on the other filters, and 37.2% (38,553) remain after filtering. The latter fraction seems to be low at first glance, but it is high compared with the 92.1% of organised precipitation cores in Germany that Pscheidt *et al.* (2019) reported from their 2-year statistics. The difference might emerge from the fact that they define organisation in terms of connectivity of single detections of precipitation cores, whereas in the study at hand the dynamical organisational form in terms of single cells, multicells, supercells, and mesoscale convective systems are referred to – similar to Markowski and Richardson (2010). Moreover, KONRAD uses a much higher operational reflectivity threshold, so that a direct and fair comparison is not possible.

2.2 | Model data: NWP model COSMO-EU

The DWD operationally used the NWP model COSMO-EU for regional weather forecasts from the end of September 2005 to November 2016. The model covers almost all of Europe with a grid point distance of 0.0625° (≈7 km). Hence, non-hydrostatic mesoscale effects are partially captured. Meanwhile, the DMC still needs to be parametrised, as do many other subgrid-scale processes. Vertically, 40 hybrid terrain-following model levels are defined, ranging from 10 m above ground to a height of 21.75 km (Schulz and Schättler, 2014).

The operational workflow at the DWD is subdivided into the data assimilation cycle and the generation of NWP analyses and forecasts. Whereas COSMO-EU NWP analyses were generated four times a day, assimilation analyses were produced within the assimilation cycle each hour. Additionally, the availability of assimilation analyses is not as time critical compared with the NWP analyses needed to initialise the corresponding forecasts. This results in a later cut-off time for observations to arrive. The observations are then considered in the assimilation analyses, and this leads to a higher analysis quality. Consequently, this study makes use of hourly assimilation analyses. Assimilation has been implemented via Newtonian relaxation (nudging), a four-dimensional procedure that pulls prognostic model variables during the forward integration of the model to observations within a predetermined time frame (Schraff, 1996; 1997; Schraff and Hess, 2013). For the period from September 2014 to November 2016, high-resolution OPERA rain rate data, which can be derived from the reflectivity factor Z, have been assimilated into COSMO-EU via additional latent heat nudging (Stephan *et al.,* 2008; DWD, 2014; Saltikoff *et al.,* 2019).

The analyses enable the calculation of a multitude of meteorological variables and convective indices that are not stored by default in the DWD database (Wilhelm, 2022). This is accomplished by extending the COSMO-EU-internal post-processing routines, initialising the model with the analyses and re-outputting the desired quantities at forecast time $t = 0$ for pressure and/or height levels. These quantities characterise different aspects of convective stability as well as air mass temperature, moisture content, and dynamical conditions (see Section 3.2). The newly implemented variables have been verified in detail by comparing them with radiosonde soundings, reanalyses, and the literature. Compared with similar studies from Europe or the United States in the context of convective events or their hazards on the basis of either coarse reanalyses (e.g., Brooks, 2009; Kaltenböck *et al.,* 2009; Ukkonen *et al.,* 2017; Westermayer *et al.,* 2017)

1477870x, 2023, 755, Downloaded from https://rmets.onlinelibrary.wiley.com/doi/10.1002/qj.4505 by Karlsruher Institution F. Technologie, Wiley Online Library on [10/11/2023]. See the Terms and Conditions (https://onlinelibrary.wiley.com/terms-and-conditions) on Wiley Online Library for rules of use; OA articles are governed by the applicable Creative Commons License

or proximity sounding data (e.g., Kunz, 2007; Mohr and Kunz, 2013; Púčik *et al.,* 2015), COSMO-EU provides a temporally and spatially high-resolution representation of the atmospheric state (Miller and Mote, 2018; Zöbisch *et al.,* 2020).

2.3 | Data combination

The object-based KONRAD life cycles are combined with the meteorological ambient variables from COSMO-EU. For this purpose, the relevant 2D and three-dimensional (3D) COSMO-EU fields are linearly interpolated to the 5-min resolution of the KONRAD data at first. Subsequently, for every time instance of the detection of a cell, a circular surrounding area is put around the respective cell. The radius of this area is determined as the composition of the radius of a circle, which encloses the cell-enframing latitude–longitude rectangle minimally, as well as the additional fixed width of $R_{\mathrm{fix}} = 25\,\mathrm{km}$, which leads to an adaptive surrounding area depending on the size of the cell detected (Appendix A.2, Figure A3). Within that area, nine statistical measures of the ambient variables are computed at the detection time (percentiles, distance-weighted and unweighted spatial averages and standard deviations). Various sensitivity studies, conducted with the focus on the described aspects for a convectively active time period in May–June 2016 (Piper *et al.,* 2016), consolidate the suitability of the chosen settings. Note that, for example, choosing an earlier time instance (e.g., 30 or 60 min before the detection time) for the computation of the pre-convective ambient conditions or culling regions of precipitation (as regions of modified ambient conditions) have only a minor qualitative effect on the statistical measures and, therefore, are omitted.

For the sake of easy reading, the indication of the statistical measure is omitted in the following, as mostly only minor differences occur in the subsequent analyses, except for standard deviations that are marked with the superscript "(sd)". Of the available ambient variables, 33 are used for further discussion to focus on the most relevant ones and to avoid redundancies (Appendix A.2, Table A1). The selection criterion is based mainly on the discrimination ability of the variables between short- and long-living cells (see Section 4). From this, 28 of the 33 variables are obtained, among them the temperature and the equivalent potential temperature (approximation for a pseudo-adiabatic process; Bolton, 1980) at the 850 hPa level: T_{850} and $\theta_{\mathrm{e},850}$. To represent air mass temperature gradients in the cells' surroundings, the standard deviations of these temperature variables $T_{850}^{(\mathrm{sd})}$ and $\theta_{\mathrm{e},850}^{(\mathrm{sd})}$ respectively, are also considered. Moreover, the well-known lifting condensation level height ($\mathrm{LCL_{MU}}$), the vertically integrated water vapour (IWV), and the stability index $\Delta\theta_{\mathrm{e}}$ (Atkins and Wakimoto, 1991) – here in the formulation of Kunz (2007) – are included as well, yielding 33 ambient variables in total.

3 | STATISTICAL PROPERTIES OF CELL ATTRIBUTES AND AMBIENT CONDITIONS

3.1 | General cell properties

This section briefly summarises the properties of the convective life cycles without any further information about their ambient conditions. Wapler (2021) already presented the multiyear life-cycle statistics of more than 100,000 KONRAD cells between 2007 and 2017, partly focusing on the 5-year period from 2013 to 2017. They mentioned that the life-cycle properties were qualitatively very similar for their long and short periods, so the 6-year period from 2011 to 2016 with the 38,553 KONRAD cells used in this study sufficiently captures the overall statistics. It should be noted, however, that the filtering of the life cycles in this study as described in Section 2.1 differs somewhat from the methods of Wapler (2021). However, the goal is the same: to analyse the undisturbed life cycles of isolated convection. In addition to the description of the general cell properties in the following paragraphs, short life-cycle analyses in the style of Wapler (2021) are presented in Appendix A.1, which motivate the selection of cell attributes and introduce mathematical descriptions.

Owing to the different types of organisation of convective storms (single cells, multicells, supercells, and mesoscale convective systems), the life-cycle characteristics of individual cells may be strongly influenced by adjacent cells, leading to ambiguous life-cycle definitions. Cell clusters and mesoscale convective systems, consisting of multiple individual convective cells, are much more difficult to track compared with isolated convective cells. The lifetime of the embedded individual cells and their spatial extent detected by KONRAD do not allow one to draw conclusions about the main characteristics of the entire cell complex. These are the main arguments for focusing on non-splitting and non-merging isolated convection, as other storms do not disturb their individual life cycles. Still, the need exists for efficient nowcasting methods that are as general as possible to obtain realistic estimates for all future cell evolutions. It is possible that the findings on isolated convection may be transferred in such a way that nowcasting methods can be improved in the prediction of other types of convective storm organisation. We recognise, however, that this remains to be proven in future studies and that tracking-based statistical investigations of

1477870x, 2023, 755, Downloaded from https://rmets.onlinelibrary.wiley.com/doi/10.1002/qj.4505 by Karlsruher Institution F. Technologie, Wiley Online Library on [10/11/2023]. See the Terms and Conditions (https://onlinelibrary.wiley.com/terms-and-conditions) on Wiley Online Library for rules of use; OA articles are governed by the applicable Creative Commons License

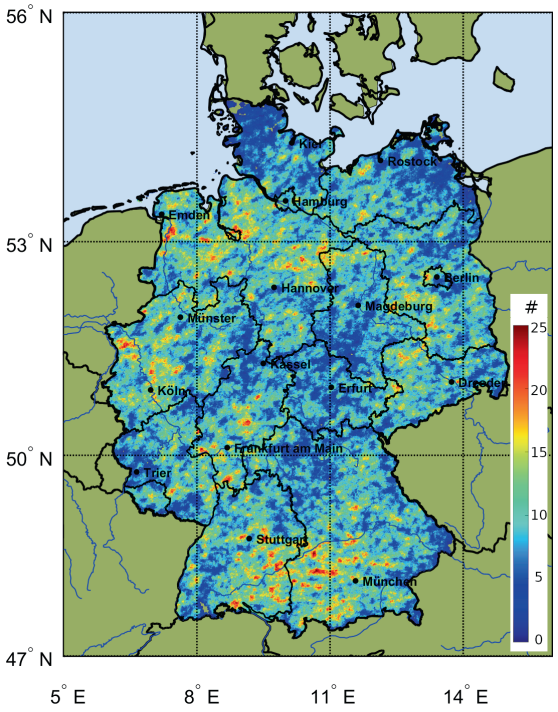


FIGURE 1 Spatial distribution of the total number of convective cells (colours) during the investigation period of the summer half-years of 2011–2016 ($1 \times 1\,km^2$ grid), derived from track polygons of cells detected via KONRAD. Only grid points over land inside of Germany are evaluated.

the life cycles of multicellular convection are needed to foster both a better understanding of the underlying mechanisms and a more sophisticated treatment of them in cell detection and tracking algorithms.

The 38,553 isolated storms of the investigation period of the summer half-years of 2011 to 2016 occurred in all parts of Germany (Figure 1). Cell tracks can approximately be represented by polygons derived from the cell-enframing latitude–longitude rectangle and direction information gathered through KONRAD (see Section 2.1). The regions in southern Germany and around Frankfurt am Main (50.1° N, 8.7° E) that exhibit comparatively high cell numbers are well known for the frequent occurrence of thunderstorms (e.g., Wapler and James, 2015; Piper and Kunz, 2017; Taszarek *et al.,* 2019). Remarkably different from storm climatology is the high number of cells in northwestern Germany that can be ascribed to the convectively active period in May–June 2016 (Piper *et al.,* 2016). The spatial distribution of the number of storm days (i.e., days with at least one storm passing by a location on a $1 \times 1\,km^2$ grid) turns out to be qualitatively and quantitatively very similar to the distribution of total cell number shown in Figure 1 (i.e., days with more than one storm at a location are rare in the dataset).

The absolute frequency distributions of cell lifetime T, maximum area during the life cycle A_{max} (Figure 2a), and track length (not shown) appear very skewed, expressing the prevalence of short-living, small cells in the dataset (Wapler, 2021). In general, long-living cells reach comparatively higher maximum cell areas and longer tracks than short-living cells do. Nevertheless, their maximum area, propagation speed, and track length may differ significantly among each other. Cells with a long lifetime of more than 60 min (1,096 cells or 2.8%) and 120 min (121 cells or 0.3%) are detected across the entire country. Note that the lifetime at the first detection is assumed to be 2 min for all cells. Owing to the strict cell definition and detection criterion of KONRAD regarding the radar reflectivity factor (see Section 2.1), which leave out considerable parts of the cells' cumulus and dissipation stage, the lifetime of a KONRAD cell can typically be considered to be shorter than the lifetime of the real convective cell. Among the 10 KONRAD cells with the longest lifetimes (up to more than 240 min) were several prominent supercells whose rotation was confirmed by eyewitnesses. Other supercells are not included owing to the filter criteria mentioned in Section 2.1, like the supercell on September 11, 2011 (Fluck, 2018), or the supercells on July 27–28, 2013 (Kunz *et al.,* 2018).

A large fraction of the cells (that increases with storm lifetime) moved from (south)westerly to (north)easterly directions. The overall direction distribution (not shown) is well in line with other radar-based tracking studies for Germany (e.g., Wapler and James, 2015; Schmidberger, 2018) and is a consequence of the favourable conditions for convection, when moist and warm air masses from the southwestern European and western Mediterranean regions are advected to central Europe (Kapsch *et al.,* 2012; Piper and Kunz, 2017; Mohr *et al.,* 2019). The propagation speed c of the cells ranges from close to zero to values above $25\,m \cdot s^{-1}$, mirroring different dynamic environments (Figure 2a). The initial cell growth is highly variable. However, the life-cycle analyses in Appendix A.1 indicate that the cell area at the first few life-cycle stages (e.g., the cell area detected 5 min after the first detection $A_{t=7\,min}$; Figure 2a) might serve as a good predictor for the cell lifetime and the maximum cell area during the life cycle. A last interesting property of the cells in the dataset is that during the life cycles of long-living cells ($T > 60$ min), many other cells are present across the country (Figure 2b). These simultaneous cells, which were each detected at least at one detection time of the respective long-living cells, were mostly short-lived due to the general majority of the short-living cells. Several of them occurred in similar ambient conditions in the wider vicinity of the long-living cells (i.e., their track centres were closer than 100 km to the long-living cells' track centre, but the cells

1477870x, 2023, 755, Downloaded from https://rmets.onlinelibrary.wiley.com/doi/10.1002/qj.4505 by Karlsruher Institution F. Technologie, Wiley Online Library on [10/11/2023]. See the Terms and Conditions (https://onlinelibrary.wiley.com/terms-and-conditions) on Wiley Online Library for rules of use; OA articles are governed by the applicable Creative Commons License

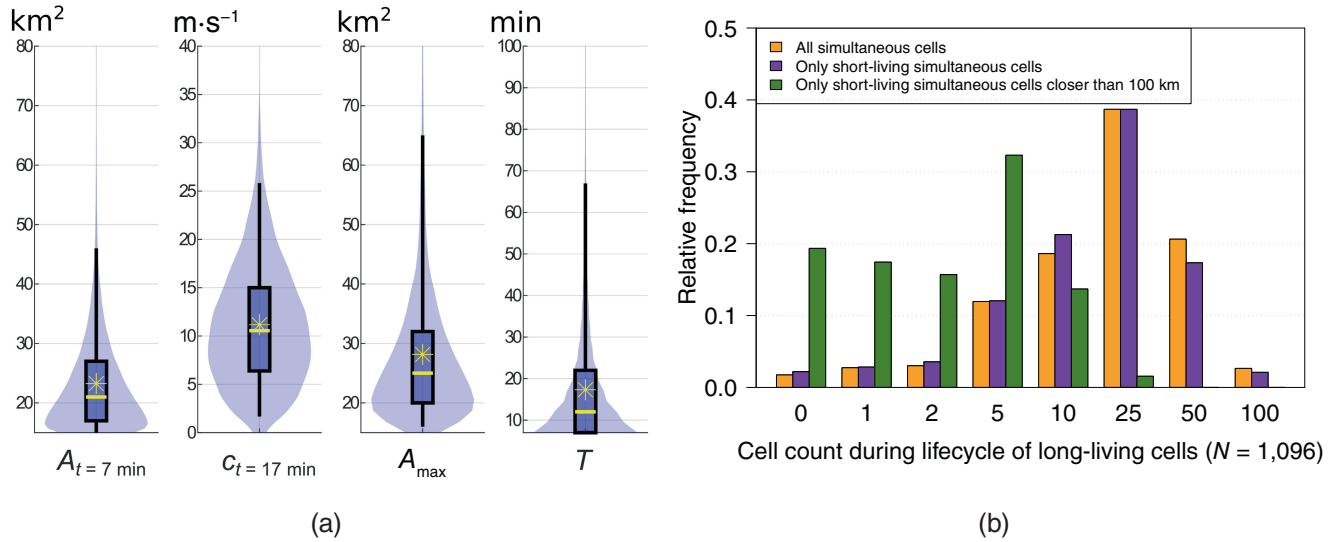


FIGURE 2 (a) Frequency distributions of the cell area detected 5 min after the first detection $c_{t=7\ min}$, propagation speed 15 min after the first detection $c(t = 17\ min)$, maximum cell area during life cycle A_{max}, and cell lifetime T. The interquartile range is highlighted by boxes, the median by the yellow line, the arithmetic mean by the yellow star and the 2nd and 98th percentiles by the whiskers. The kernel density estimation of the distribution according to Parzen (1962) was applied with a Gaussian kernel. (b) Relative frequency of the simultaneous cell count during the life cycles of the 1,096 long-living cells with lifetime $T > 60$ min. Bars for all simultaneous cells (orange), only short-living simultaneous cells (purple), and short-living simultaneous cells within a spatial circle with 100 km radius (green) are depicted. The numbers on the abscissa indicate the top limit of the respective interval.

did not interact), so that around 80% of the long-living cells were accompanied by at least one short-living cell each, and around 50% were accompanied by at least three short-living cells each.

3.2 | Characteristics of ambient variables

The analyses presented in this section investigate the properties of the ambient variables prevailing during the occurrence of the detected convective cells but without any relation to life-cycle attributes, such as lifetime or maximum cell area. As described in Section 2.3, the subsequent evaluations focus on the 33 most relevant ambient variables. Their values reflect mean values averaged over the respective cell lifetime, as the analyses revealed that their variations along the cell track are in many cases negligibly small (see later), especially for short-living cells, which constitute most of the event set. The ambient variables comprise several parameters characterising ambient dynamics (wind and vertical wind shear), thermodynamical parameters representing convective stability, moisture and temperature quantities, characteristic levels from parcel theory (e.g, Bjerknes, 1938; Holton, 2004) and composite parameters consisting of a combination of several quantities. A complete list of the 33 variables, including their long and short names, is given in Appendix A.2 (Table A1).

The frequency distributions of seven of the 33 variables mirror the range of atmospheric conditions in which the 38,553 storms occurred (Figure 3a). Only parameters frequently used for the description of thunderstorm environments in the ingredients-based forecasting (see Section 1) are discussed: the most unstable (MU) convective available potential energy $CAPE_{MU}$, the 700–500 hPa lapse rate $LR_{700-500}$, the mixed-layer (ML; lowest 100 hPa) lifted index LI_{ML}, the 0°C-level height $h_{0°C}$, the IWV, the deep-layer shear DLS, and the 0–3 km storm relative helicity SRH_{0-3} calculated using the parametrisation of Bunkers *et al.* (2000) for right-movers. About 74% of the cells occurred in thermodynamical conditions with $CAPE_{MU} < 500\ J{\cdot}kg^{-1}$, corresponding to a theoretical maximum updraught velocity of $W_{MAX} = (2CAPE_{MU})^{1/2} \approx 32\ m{\cdot}s^{-1}$ (e.g., Markowski and Richardson, 2010). Only 7% of the cells evolved during high $CAPE_{MU}$ with values above $1{,}000\ J{\cdot}kg^{-1}$. High CAPE values are climatologically observed on fewer days or hours per year in central Europe compared with the United States (Brooks *et al.*, 2003; Taszarek *et al.*, 2020). The $LR_{700-500}$, a differential measure of midtropospheric convective instability, ranges mostly between typical values of 5.5 and 6.5 $K{\cdot}km^{-1}$ (Westermayer *et al.*, 2017), whereas larger values are represented sparsely. The values of LI_{ML}, another measure of convective instability, mostly range from −4 K (unstable) to +2 K (stable). A positive LI_{ML} does not necessarily imply a stable stratification, as an air parcel starting to rise

1477870x, 2023, 755, Downloaded from https://rmets.onlinelibrary.wiley.com/doi/10.1002/qj.4505 by Karlsruher Institution F. Technologie, Wiley Online Library on [10/11/2023]. See the Terms and Conditions (https://onlinelibrary.wiley.com/terms-and-conditions) on Wiley Online Library for rules of use; OA articles are governed by the applicable Creative Commons License

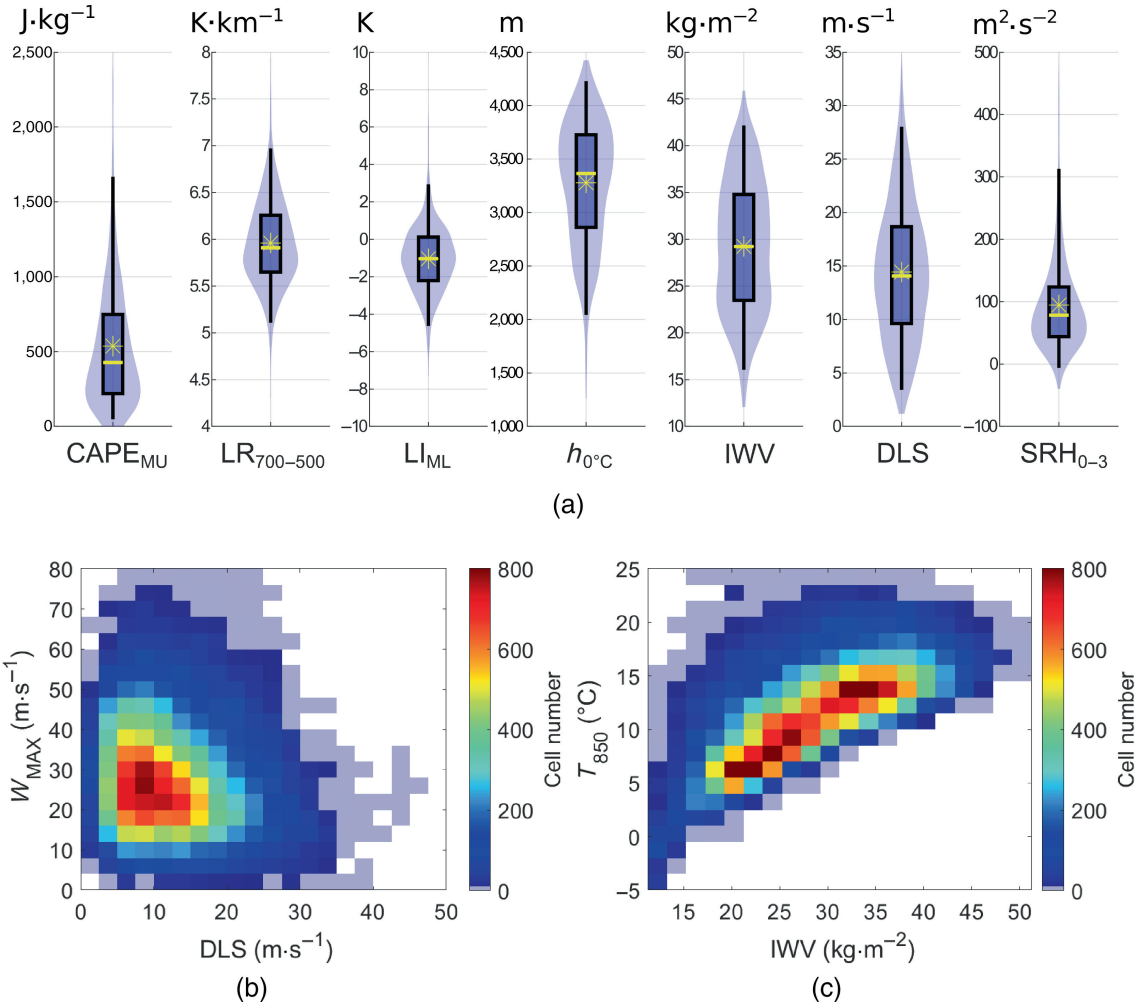


FIGURE 3 (a) Similar to Figure 2a, but showing frequency distributions of a selection of seven atmospheric variables (from left to right): most unstable convective available potential energy ($CAPE_{MU}$), 700–500 hPa lapse rate ($LR_{700-500}$), mixed-layer lifted index (LI_{ML}), 0°C-level height ($h_{0°C}$), vertically integrated water vapour (IWV), deep-layer shear (DLS), 0–3 km storm relative helicity (SRH_{0-3}). (b, c) Combined frequency distributions for the ambient conditions, (b) for the combination of DLS and maximum updraught velocity $W_{MAX} = (2CAPE_{MU})^{1/2}$, and (c) for the combination of IWV and 850 hPa temperature (T_{850}). Value ranges with fewer than 10 assigned cells are shown transparently.

from a higher or more unstable level than the averaged ML may still have experienced positive buoyancy. LI values below −5 K usually come with very high CAPE values of more than 1,000 J·kg^{-1} (Westermayer *et al.,* 2017) and are only sparsely represented in the dataset. As most of the 38,553 cells have a short lifetime (see Section 3.1), the temporal variability of the ambient variables during the life cycle is rather small compared with the general variability between the different storm environments (in terms of standard deviation). Nevertheless, this ratio of life-cycle variability to environment variability is occasionally >1 for long-lasting cells, especially for thermodynamical quantities, such as CAPE and LI, which typically vary on comparatively small scales. In addition, the ratio is sensitive to temperature and moisture variations in the near-surface tropospheric layers (Lee, 2002; Miller and Mote, 2018).

About 19% of the cells experienced a rather strong vertical wind shear, with DLS values being higher than 18 m·s^{-1}, which are favourable for potential supercell developments (Markowski and Richardson, 2010). Most of the cells occurred in rather calm to moderate dynamical conditions with DLS values below 18 m·s^{-1}, a range where extreme convection-related hazards are only occasionally observed (except for heavy rain from stationary storms, which are especially favoured by such conditions; Púčik *et al.,* 2015; Aregger, 2021). The SRH_{0-3} is mostly in the range 0–150 m^2 ·s^{-2} (Taszarek *et al.,* 2020). In conclusion, the bulk of the cells analysed represents single cells in weak to moderate dynamical and thermodynamical conditions (Figure 3b), which can be partly explained by the application of the cell filters described in Section 2.1. Especially in warm summer air masses (850 hPa temperature

1477870x, 2023, 755, Downloaded from https://rmets.onlinelibrary.wiley.com/doi/10.1002/qj.4505 by Karlsruher Institution F. Technologie, Wiley Online Library on [10/11/2023]. See the Terms and Conditions (https://onlinelibrary.wiley.com/terms-and-conditions) on Wiley Online Library for rules of use; OA articles are governed by the applicable Creative Commons License

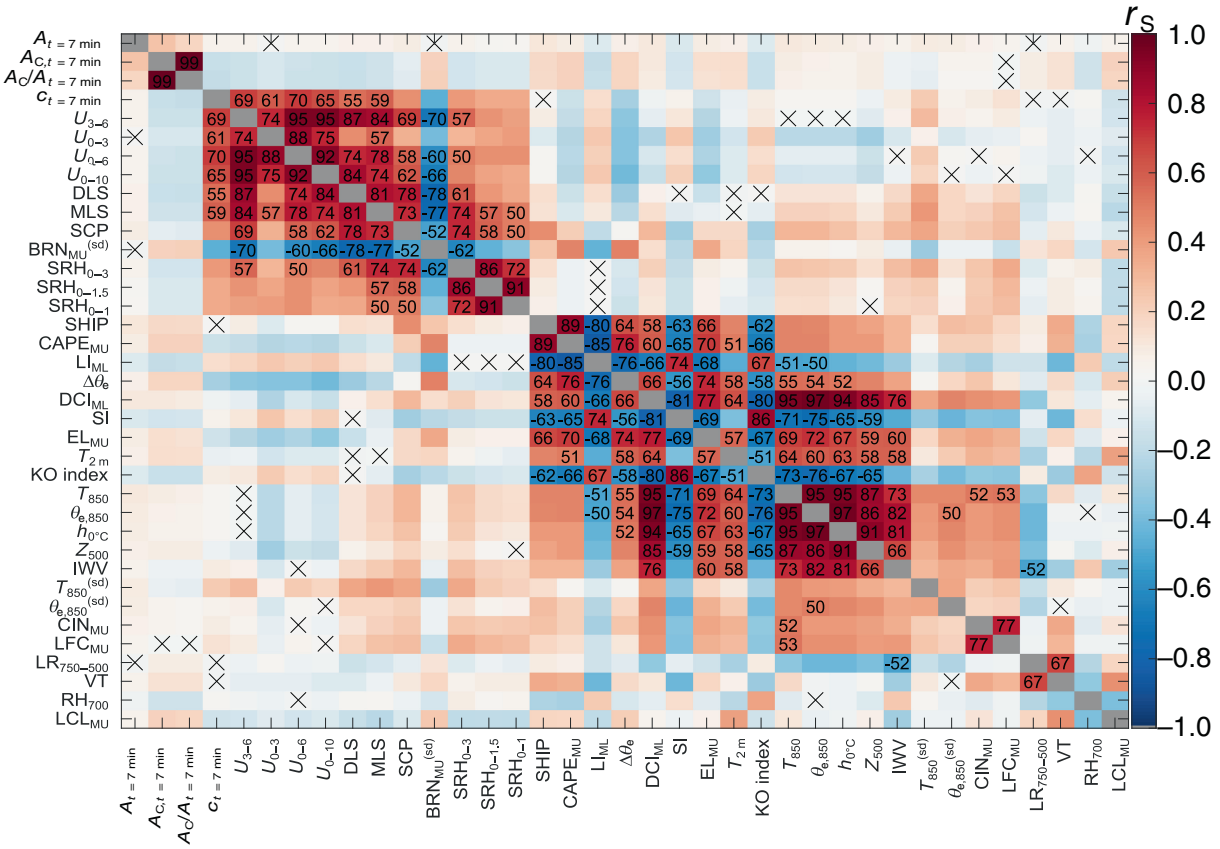


FIGURE 4 Correlation matrix of Spearman's rank correlation coefficient r_S (colours) for the 33 selected ambient variables as well as the cell attributes area A, core area A_C, their ratio A_C/A, and propagation speed c 5 min after the first cell detection ($t = 7$ min). For an explanation of the abbreviations used for the ambient variables, please refer to Table A1 in Appendix A.2. High (anti-)correlations are shown in strong hues (red: $r_S > 0$; blue: $r_S < 0$), low ones in pale hues. (Anti-)correlations with an absolute value equal to or above 0.5 are additionally given as numerical values (percent). Statistically insignificant correlations are marked with a cross (significance level $P = 0.01$).

T_{850} higher than 10–15°C), the IWV reaches high values mostly ranging from 25 kg·m^{-2} to more than 40 kg·m^{-2} as a consequence of the Clausius–Clapeyron relation (Figure 3c). These are remarkable values that can lead to heavy precipitation and flooding (e.g., Wilhelm *et al.*, 2021). Regarding the spatial variability of the ambient conditions, only several thermodynamical quantities vary on the meso-α scale (Orlanski, 1975) conspicuously, indicating a northwest-to-southeast gradient (e.g., the average $\mathrm{LI_{ML}}$ decreases, and T_{850} and $h_{0°C}$ remarkably increase from northwest to southeast), which mirrors the general mean air mass distribution over Germany during summertime (not shown).

3.3 | Correlation and cluster analysis

The (anti-)correlation in terms of Spearman's rank correlation coefficient r_S between either two dynamical or two thermodynamical quantities is high and significant for many combinations (Figure 4; Manzato, 2012; Ukkonen and Mäkelä, 2019). The agglomerations of correlation coefficients apparent in Figure 4 can be further interpreted by non-hierarchical correlation clustering, an objective multivariate correlation approach. The *k*-medoids clustering, akin to the extensively used *k*-means clustering, is able to find clusters of correlated variables based on the dissimilation matrix alone without knowing the space dimensionality and the positions of the variables in this space (MacQueen, 1967; Lloyd, 1982; Kaufman and Rousseeuw, 1990). The corresponding algorithm is called "partitioning around medoids", which converges with arbitrary dissimilation metrics. Here, the measure $d = 1 - |r_S|$ serves as a dissimilation metric: d is small for strong bivariate (anti-)correlations and is close to 1 for weak correlations (Van der Laan *et al.*, 2003). The quality of the clustering is assessed by means of silhouette coefficients, with $S \to 1$ representing strong structuring and $S < 0$ indicating the need for the improvement of the clustering (Rousseeuw, 1987).

The highest total silhouette coefficient with $S = 0.42$ is reached for $N_C = 4$ clusters (Figure 5). However, clustering

1477870x, 2023, 755, Downloaded from https://rmets.onlinelibrary.wiley.com/doi/10.1002/qj.4505 by Karlsruher Institution F. Technologie, Wiley Online Library on [10/11/2023]. See the Terms and Conditions (https://onlinelibrary.wiley.com/terms-and-conditions) on Wiley Online Library for rules of use; OA articles are governed by the applicable Creative Commons License

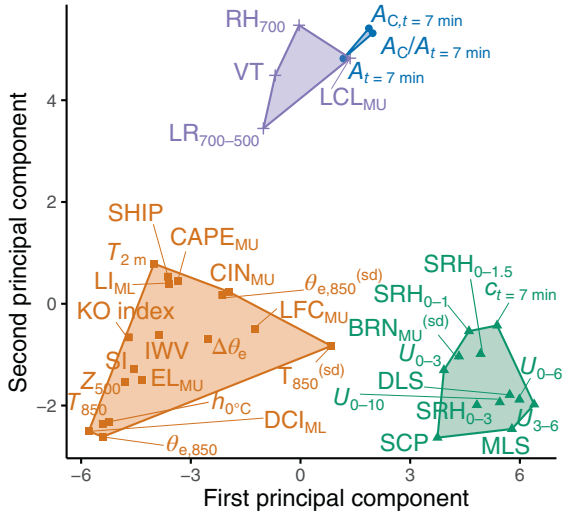


FIGURE 5 Representation of $N_C = 4$ clusters of ambient variables and cell attributes identified by a k-medoids clustering. The dissimilation metric is $d = 1 - |r_S|$. The projection of the clusters onto the first two principal axes of the high-dimensional eigenspace after multidimensional scaling is shown. The first principal axis explains 46.5% of the observed variability, and the second principal axis explains 17.7% of the observed variability.

into three to seven clusters yields very similar values (e.g., $S = 0.37$ for $N_C = 7$). The clustering with $N_C = 4$ reveals one cell (core) area cluster, one dynamical cluster at positive values of the first principal axis (mirroring the top left ambient variable agglomeration in Figure 4 including the cell propagation speed), and two clusters consisting of thermodynamical and moisture quantities. Note that analogous clustering without cell attributes yields the same constitutions of the three ambient variable clusters. The medoids – that is, the variables whose average dissimilarity to all variables in the four respective clusters is minimal (they can thus be considered to be their respective nuclei) – are $A_{C,t=7\,min}$, the midtropospheric mean wind between 3 and 6 km above ground level ($U_{3–6}$), the vertical totals index (VT), and the ML deep convective index (DCI_{ML}). Thereby, the clusters represent the cell (core) area attributes, the midtropospheric flow, differential convective instability in the middle troposphere as well as a collection of air mass temperature, moisture, and further convective instability indices. Note that the medoids do not necessarily have to look centred in the clusters in Figure 5, as only the projection onto the first two principal axes of the high-dimensional eigenspace after multidimensional scaling (Pison *et al.*, 1999) is depicted. The three ambient variable clusters are reminders of the best discriminator between the high-shear low-CAPE severe and non-severe convective events of Sherburn and Parker (2014): the severe hazards in environments with reduced buoyancy (SHERB) parameter, which multiplicatively consists of a wind (shear) parameter, a midlevel lapse rate, and a low-level lapse rate.

Within the thermodynamical cluster, for example, the anti-correlation between the integral and differential stability measures $CAPE_{MU}$ and LI_{ML}, as adumbrated by analyses from Westermayer *et al.* (2017), is strong with $r_S = -0.85$. Additionally, the principal component analysis between W_{MAX} and LI_{ML} reveals that the first principal component explains more than 90% of the total variance (not shown). This is a stronger anti-correlation as found by Manzato (2012) and Mohr and Kunz (2013) between different CAPE definitions and the LI. The differences presumably emerge from the fact that the latter studies are based on parameters stemming from proximity soundings (i.e., real radiosonde measurements), which are compared with parameters derived from analysis data of an imperfect convection-parametrising model here. Nevertheless, the model-derived parameters describe the reality sufficiently well, and have the advantage that they represent the conditions in an environment and at a time instance, which are close to the observed storm occurrence (see Section 2.3).

Within the dynamical cluster, DLS is moderately correlated with $SRH_{0–3}$ ($r_S = 0.62$). A very strong correlation exists between DLS and the midtropospheric mean wind $U_{3–6}$ ($r_S = 0.87$), whereas its correlation with the lower tropospheric mean wind between 0 and 3 km $U_{0–3}$ is remarkably smaller ($r_S = 0.45$). As the correlation of DLS and the midtropospheric wind at the 500 hPa level U_{500} (a variable not used for further evaluation and discussion) is even higher with $r_S = 0.91$, it can be concluded that DLS seems to be mainly determined by the absolute value of the midtropospheric wind. All conclusions in the following sections that are drawn based on DLS could therefore be virtually attributed to the midtropospheric wind. The cell propagation speed $A(t = 7\,min)$ exhibits a higher correlation with the vertically averaged mean wind (e.g., $r_S = 0.70$ with $U_{0–6}$) than with the vertical shear (e.g., $r_S = 0.55$ with DLS). The supercell composite parameter (SCP; Thompson *et al.*, 2003), which is multiplicatively composed of $CAPE_{MU}$, DLS, and $SRH_{0–3}$, and which is calculated as in the formulation of Gensini and Tippett (2019), is more strongly correlated to dynamical than to thermodynamical parameters. The same applies for the spatial standard deviation of the MU bulk Richardson number $BRN^{(sd)}_{MU}$, which represents the variability of the ratio between potential and kinetic energy in the cells' surroundings (Markowski and Richardson, 2010). In contrast, the significant hail parameter (SHIP; NOAA SPC, 2014), which consists of $CAPE_{MU}$, DLS, the water vapour mixing ratio, and the midtropospheric lapse rate and temperature, as used, for instance, in Prein and Holland (2018), Czernecki *et al.* (2019), and Tang *et al.* (2019), correlates more with thermodynamical quantities.

1477870x, 2023, 755, Downloaded from https://rmets.onlinelibrary.wiley.com/doi/10.1002/qj.4505 by Karlsruher Institution F. Technologie, Wiley Online Library on [10/11/2023]. See the Terms and Conditions (https://onlinelibrary.wiley.com/terms-and-conditions) on Wiley Online Library for rules of use; OA articles are governed by the applicable Creative Commons License

Within the cell (core) area cluster, it is apparent that cell core area A_C dominates the ratio A_C/A, which can be largely attributed to the fact that $A_{C,t=7\,\mathrm{min}}$ has mostly small values (e.g., 0 km^2 for approximately 60% of the cells). Interestingly, the correlations of all variables with $A_{t=7\,\mathrm{min}}$ are weak ($|r_S| \leq 0.1$) except for its correlation with SHIP, which is slightly higher. The strongest cross-cluster correlation is $r_S = -0.52$ for IWV and $LR_{700-500}$, which is even stronger than the correlation is between IWV and the relative humidity at the 700 hPa level RH_{700}. Moreover, the latter is the ambient variable with the most weak correlations ($|r_S| \leq 0.1$) with other ambient variables. Further cross-cluster correlations with $|r_S| > 0.4$ comprise the thermodynamical combinations of $LR_{700-500}$ with $h_{0°C}$ or $\theta_{e,850}$, as well as VT with LI_{ML} or Showalter index SI. A low correlation exists, however, between DLS and LI_{ML} ($r_S = 0.19$), mirroring the plausible weak connection between the vertical wind shear and convective instability. The highest (anti-)correlations between a dynamical and a thermodynamical variable can be reported for the combinations of the medium-layer shear (MLS) with $T_{850}^{(sd)}$ ($r_S = 0.42$), and U_{0-10} with $\Delta\theta_e$ ($r_S = -0.41$).

Incorporating more than the chosen 33 ambient variables into the clustering identifies that further midtropospheric thermodynamical and moisture variables can be related to the cluster at large positive values of the second principal axis. For example, building seven clusters splits the dynamical cluster into an SRH cluster and the remaining quantities, whereas from the thermodynamical cluster at negative values of the first principal axis, two smaller clusters are separated. Building even more clusters separates A from A_C and A_C/A and increasingly produces further single-variable clusters, which should be avoided. It is difficult to determine which cluster number between 3 and 7 is thus most appropriate. For the study at hand, $N_C = 4$ is chosen for further evaluations. In conclusion, the results from the clustering procedure enable a fast and concise overview of the correlations and the correlation-based distance, respectively, between a variable and many others (compared with the correlation matrix in Figure 4). Moreover, it can serve as an objective decision basis to omit redundant information and select suitable combinations of rather independent ambient variables for multivariate analyses and forecasts of convective cell evolution.

4 | STATISTICAL RELEVANCE OF AMBIENT CONDITIONS FOR CELL EVOLUTION

The analyses presented in this section examine the life-cycle attributes lifetime T and the maximum cell area A_{max} and their relations with the prevailing ambient variables, as well as with the cell attributes cell area A, core area A_C, their ratio A_C/A, and propagation speed c (at specific cell ages), in the following referred to as predictors. As in Section 3, the evaluations consider the 33 most relevant ambient variables (see Appendix A.2, Table A1). The univariate analyses in Section 4.1 comprise not only investigations of the discrimination skill between short- and long-living cells for the set of predictors (Section 4.1.1) but also a similar examination of the discrimination between small and large cells with respect to their maximum cell area during the life cycle (Section 4.1.2). In addition, Section 4.1.3 presents a simple mathematical model for the description of the evolution of the cell area, considering information about an ambient variable for the example of LI_{ML}. Bivariate analyses demonstrating quantitatively the statistical connections between cell attributes and the combinations of two predictors complete this section (Section 4.2).

4.1 | Univariate analyses

4.1.1 | Discrimination of cell lifetime classes

First, the predictors are evaluated with regard to their ability to distinguish between short- and long-living cells. The lifetime separator for the following discussion is $\tau = 60$ min, separating the data into 37,457 short-living (i.e., $T \leq 60$ min) and 1,096 long-living ($T > 60$ min) cells. Generally, the separator value may be chosen arbitrarily, resulting in potentially different outcomes. Thus, the discriminator just defined is one possibility focusing on the peculiarities of the ambient conditions of the 2.8% longest-living cells, whose lifetime is well above the typical values of usually not very severe single cells.

Following the methodology of Czernecki *et al.* (2019), an estimation of the distribution function (probability density function, PDF) of these two classes is made via the kernel density estimation according to Parzen (1962) with a Gaussian kernel and 100 interpolation points. Moreover, several scores based on categorical verification (e.g., Mason, 1982; Wilks, 2006) are considered for the evaluation of the predictor skills. These include the probability of detection POD and the probability of false detection POFD (also known as the hit and false alarm rate), the Peirce skill score PSS = POD − POFD, and the parameter d', which indicates the separation of two distributions in terms of the number of standard deviations that the means of the two distributions are apart (assuming normal distributions with equal standard deviations; higher values of d' indicate an easier discrimination; Brooks and Correia, 2018). These

1477870x, 2023, 755, Downloaded from https://rmets.onlinelibrary.wiley.com/doi/10.1002/qj.4505 by Karlsruher Institution F. Technologie, Wiley Online Library on [10/11/2023]. See the Terms and Conditions (https://onlinelibrary.wiley.com/terms-and-conditions) on Wiley Online Library for rules of use; OA articles are governed by the applicable Creative Commons License

TABLE 1 Contingency table explaining hits, false alarms, misses, and correct rejections for the analysis of lifetime discrimination, using the example of the deep-layer shear (DLS) as predictor.

	Long-living	Short-living
Above DLS threshold	Hit	False alarm
Below DLS threshold	Miss	Correct rejection

scores can be depicted in the receiver operating characteristic (ROC) diagram. Moreover, the POD, the success ratio SR = 1 − FAR (where FAR is the false alarm ratio), the critical success index (CSI), and the bias B are used to describe the predictive skill in performance diagrams. For example, the fraction of long-living cells associated with a high DLS above a certain DLS threshold (hits) defines POD, whereas the fraction of short-living cells associated with a high DLS above this threshold (false alarms) defines POFD (see Table 1). The FAR characterises the reliability by giving the percentage of false alarms compared with all (short- and long-living) cells above the threshold. CSI relates the number of hits to all cells that are above the DLS threshold or long-living cells (i.e., all but the correct rejections). The bias B relates the number of forecasted long-living cells to the number of observed long-living cells. For variables with decreasing values for a longer lifetime (e.g., LI_{ML}), the scores are defined with respect to the reversed threshold behaviour (i.e., "above" and "below" in Table 1 are swapped). The optimal thresholds of the predictors are tested iteratively and determined such that the PSS is maximised for the ROC diagram (Manzato, 2007), and the CSI is maximised for the performance diagram. The values of the other scores in the respective diagrams relate to that same optimised threshold. The score values depend on the lifetime separator τ as alluded to earlier herein (Wilhelm, 2022). For example, PSS values generally increase for increasing values of τ, mainly due to an increase in POD. CSI values generally decrease for increasing τ due to the increasing number of cells that are defined as short-living and are not correctly assigned. Note that such a categorical evaluation forms a hard decision boundary, where, for example, cells with a lifetime of 57 min, which are forecasted to be long-living, are rated as wrongly forecasted.

The detailed PDFs from the kernel density estimation of three exemplary predictors $A_{t=7\,\mathrm{min}}$, DLS, and LI_{ML}, separately for short- ($T \leq \tau$) and long-living cells ($T > \tau$), illustrate that the higher the PSS is the lower is the resulting overlap of the PDFs (see Figure 6a–c). The PDFs contain all 38,553 cells with a minimum lifetime of 7 min. In general, the optimal variable threshold yielding the highest PSS value differs from the one for the highest CSI value. However, the overlap between the distributions for all variables is remarkably high and PSS and CSI values low, indicating only a weak discrimination and prediction skill. This will be discussed in detail in the next paragraph by means of the ROC and performance diagrams, where the different score metrics are summarised for the best variables of the four respective clusters from Figure 5 (i.e., only the results for one variable per cluster maximising PSS and CSI are shown for the sake of clarity). The dependence of the scores on the minimum cell age (i.e., on the time point when the lifetime estimation is made) will also be investigated. Individual score values and variable thresholds for all predictors are listed in the Supporting Information (Tables S1 and S2).

The ROC and performance diagram clearly show that the discrimination and prediction skill of all clusters is rather low (Figure 7). However, the (blue) cell (core) cluster achieves the best scores, followed by the (green) dynamical cluster. The (red) thermodynamical and the (purple) midtropospheric clusters show very little skill. The best predictor in terms of PSS (ranging from 0.28 to 0.38 depending on the minimum cell age) and CSI (ranging from 0.07 to 0.38) is cell area A (see Supporting Information Tables S1 and S2), represented by the markers of the cell (core) cluster. Within the dynamical cluster, several variables, such as DLS, SCP, MLS, and U_{3-6}, reach similar score values, whereas cell propagation speed c shows slightly less skill. None of the ambient variables exceeds PSS = 0.18. Owing to the majority of cells with short lifetimes, the CSI and SR values are generally rather small. This is especially true for high lifetime separator values, like $\tau = 60$ min, because many more wrong assignments of the short-living cells exist in absolute numbers compared with the correct assignments of the 1,096 long-living cells. Generally, the scores indicate only a fair discrimination and a low reliability for deriving the cell lifetime from a specific predictor during the first 37 min of the life cycle. However, CSI and SR increase with increasing cell age (e.g., for cell area A from CSI = 0.07 for predictions at $t = 7$ min, to CSI = 0.38 for predictions at $t = 37$ min), indicating a slightly more reliable estimation when the forecast time point approaches lifetime separator $\tau = 60$ min. Only the predictors from the cell (core) cluster reach CSI values that are by around 0.05–0.10 higher than those from a reference forecast, which always predicts long-living cells (Supporting Information Table S2). Thus, the gain in forecast performance is only little, when information about a single ambient variable is considered. Interestingly, the discrimination skill of the ambient variables in terms of PSS decreases slightly with increasing cell age (as does the bias B), whereas the skill for A (and A_C) increases. Hence, a strong initial cell growth and intensification seems to have positive effects on the cell lifetime

1477870x, 2023, 755, Downloaded from https://rmets.onlinelibrary.wiley.com/doi/10.1002/qj.4505 by Karlsruher Institution F. Technologie, Wiley Online Library on [10/11/2023]. See the Terms and Conditions (https://onlinelibrary.wiley.com/terms-and-conditions) on Wiley Online Library for rules of use; OA articles are governed by the applicable Creative Commons License

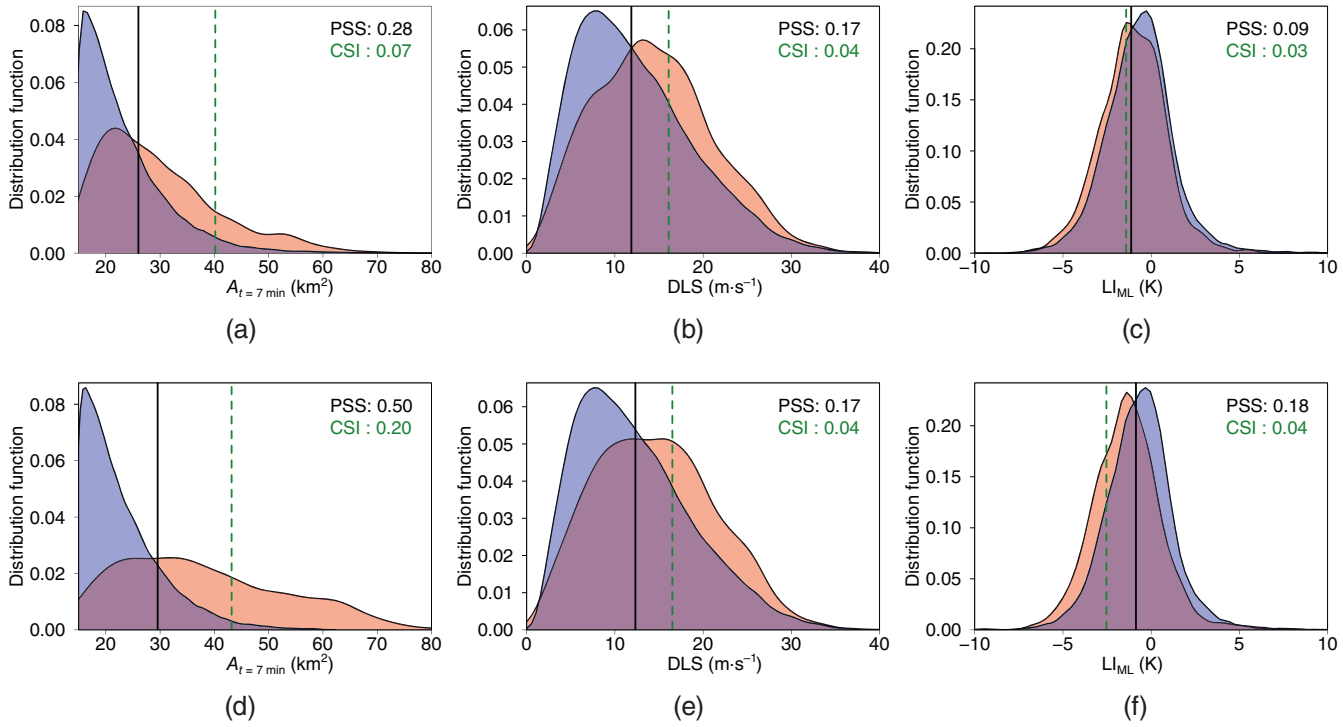


FIGURE 6 Comparison of probability density functions (PDFs) from kernel density estimation of all 38,553 cells for the three predictors cell area detected 5 min after the first detection ($A_{t=7\,\mathrm{min}}$), deep-layer shear (DLS), and mixed-layer lifted index ($\mathrm{LI_{ML}}$); (a)–(c) 37,457 short-living (blue) and 1,096 long-living (red) cells for the lifetime separation $\tau = 60$ min; (d)–(f) 37,443 small (blue) and 1,052 large (red) cells for the maximum area separation $\chi = 60\,\mathrm{km}^2$. The overlap of the PDFs appears purple. The black vertical solid line illustrates the optimal variable threshold based on the Peirce skill score (PSS), the green dashed line illustrates the optimal variable threshold based on the critical success index (CSI). The PDFs from the kernel density estimation are normalised so that the area under the graph equals 1 (i.e., their function values are unit dependent). (a)–(c) are discussed in Section 4.1.1, and (d)–(f) in Section 4.1.2.

(see Appendix A.1). Moreover, this finding suggests that, with increasing cell age, information about the cell history becomes more important compared with the ambient variables.

The optimal variable thresholds in terms of PSS, as exemplarily shown for $A_{t=7\,\mathrm{min}}$, DLS, and $\mathrm{LI_{ML}}$ in Figure 6a–c, mostly do not change much with increasing cell age (not shown) due to the minority of the 1,096 long-living cells in the statistics (i.e., the majority of the short-living cells dominate the threshold determination). The thresholds for cell area A range from 26 to 30 km^2, and the thresholds for dynamical variables represent moderate wind speed and shear conditions (e.g., DLS and U_{3-6} are around 12 m·s^{-1}), whereas the thermodynamical indices VT, KO index, SI, and $\mathrm{LI_{ML}}$ lie in the range of slightly unstable stratification (e.g., $\mathrm{LI_{ML}}$ and SI are around −1 K). The optimal variable thresholds in terms of CSI, also shown in Figure 6a–c for a few examples, change towards values that are less favourable for a long lifetime with increasing minimum cell age (e.g., thresholds for A, DLS, and U_{3-6} decrease and for $\mathrm{LI_{ML}}$ and SI increase). The better performance of the dynamical variables compared with the other two ambient variable clusters suggests that they have the best discrimination skill with respect to the lifetime due to their influence on the degree of cell organisation. This finding is in line with theoretical considerations in classical textbooks (e.g., Markowski and Richardson, 2010; Trapp, 2013) and corresponds to a higher probability of severe weather occurring in dynamically active environments (Taszarek *et al.*, 2020), which is mostly attributed to long-living convective storms. Interestingly, this result contrasts the recent finding of Zöbisch *et al.* (2020), which found no connection between DLS and cell lifetime for a set of satellite-based thunderstorm detections over central Europe. They mentioned, however, that this might originate from the fact that they deliberately did their analysis without a filtering for complete undisturbed cell life cycles in order to represent the full convective spectrum.

4.1.2 | Discrimination of cell area classes

For the investigation of the discrimination skill of the predictors with regard to classes of the maximum cell area, a similar split of the data as for the cell lifetime in

1477870x, 2023, 755, Downloaded from https://rmets.onlinelibrary.wiley.com/doi/10.1002/qj.4505 by Karlsruher Institution F. Technologie, Wiley Online Library on [10/11/2023]. See the Terms and Conditions (https://onlinelibrary.wiley.com/terms-and-conditions) on Wiley Online Library for rules of use; OA articles are governed by the applicable Creative Commons License

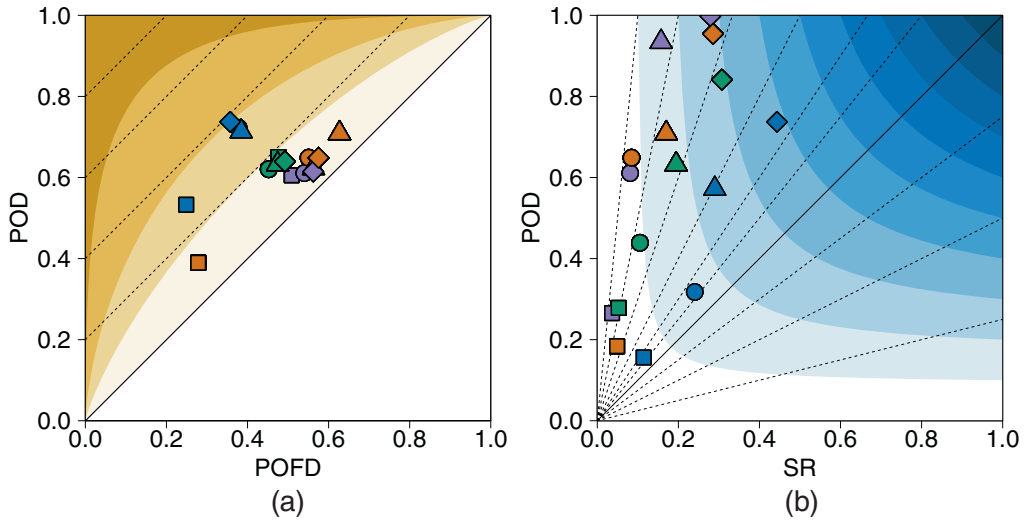


FIGURE 7 Evaluation diagrams of different score metrics for the discrimination between short- and long-living cells ($\tau = 60$ min). (a) Receiver operating characteristic diagram with the theoretical Peirce skill score PSS = 0 isoline (black) and further isolines of PSS (dashed; increasing from 0 to 1 in the top-left corner in intervals of 0.2) overlaid. Yellowish colours indicate values of d', which increase for darker hues (d': 0.5, 1.0, 2.0). (b) Performance diagram with isolines of bias (dashed; increasing from 0 in the bottom-right corner to infinity in the top-left corner; solid: $B = 1$) overlaid. Bluish colours indicate values of critical success index (CSI), which increase for darker hues (in intervals of 0.1). In both diagrams, each marker corresponds to the skill of one variable per cluster for the variable with maximum (a) PSS and (b) CSI, where the colouring is chosen in accordance with Figure 5 (blue: cell [core] area cluster; green: dynamical cluster; red: thermodynamical cluster; purple: midtropospheric cluster). The different marker shapes indicate the evaluation for different minimum cell ages (prediction time points): rectangle, 7 min ($N = 38{,}553$); circle, 17 min ($N = 15{,}094$); triangle, 27 min ($N = 7{,}148$); diamond, 37 min ($N = 3{,}942$). Ambient variable values were chosen as the life-cycle average. Cell attribute values were chosen at the respective cell ages. The best predictors of the respective clusters can be read from Supporting Information Tables S1 and S2 (underlined, bold score values). POD, probability of detection; POFD, probability of false detection; SR, success ratio.

Section 4.1.1 is performed by separating the 1,052 largest cells (2.7%), which reached maximum cell area A_{max} of more than $\chi = 60\,km^2$. For the prediction times 17 min, 27 min, and 37 min, only 1,043, 979, and 867 large cells respectively remain, as a few large cells had a short lifetime. As for the lifetime discrimination, individual score values and variable thresholds for all predictors are listed in the Supporting Information (Tables S3 and S4).

From Figure 8a, it can be seen that here, the cell (core) cluster shows a high discrimination skill (PSS ranges between 0.49 and 0.59), much higher than all ambient variables, resulting in less overlap of the corresponding PDFs (see examples in Figure 6d–f). The threshold of A that best discriminates the maximum cell area is around $A(t) = 30$–$38\,km^2$ for most prediction time points (see Figure 6d; Supporting Information Table S3). CSI and SR reach higher values than for the lifetime estimation but saturate after $t = 17$ min (i.e., the predictions after 27 and 37 min are not improving much; Figure 8b). The bias B is close to 1 for all prediction times. Like the cell area, the core area A_C and the ratio A_C/A reach better score values than all ambient variables do (Supporting Information Tables S3 and S4). In summary, these results indicate that a cell should grow strongly already during the first life-cycle stages to reach a large area during its life cycle as also Figure A1 in Appendix A.1 suggests.

In contrast to lifetime discrimination (see Section 4.1.1), when it comes to distinguishing small and large cells, thermodynamical indices reach PSS values comparable to the dynamical variables (Figure 8a; Supporting Information Table S3). Higher instability is conducive for free buoyancy-driven convection, which favours the growth of convective cells. In particular, the combined parameters SCP and SHIP, consisting of both thermodynamical and dynamical quantities, show the best discrimination but with relatively small variable thresholds below 0.25. Such values are observed very often in thunderstorm environments. PSS hardly exceeds 0.20, B is somewhat closer to 1 for all clusters, and CSI reaches values comparable to the lifetime discrimination (which are again very small when compared with the reference forecast, which always predicts cells with a large maximum cell area; Figure 8b; Supporting Information Table S4). The optimal variable thresholds for DLS and LI_{ML} do only differ slightly from the ones for the lifetime discrimination (Figure 6e,f; Supporting Information Tables S3 and S4).

Thus, compared with the skill for lifetime discrimination, the cell attributes are of higher relative

1477870x, 2023, 755, Downloaded from https://rmets.onlinelibrary.wiley.com/doi/10.1002/qj.4505 by Karlsruher Institution F. Technologie, Wiley Online Library on [10/11/2023]. See the Terms and Conditions (https://onlinelibrary.wiley.com/terms-and-conditions) on Wiley Online Library for rules of use; OA articles are governed by the applicable Creative Commons License

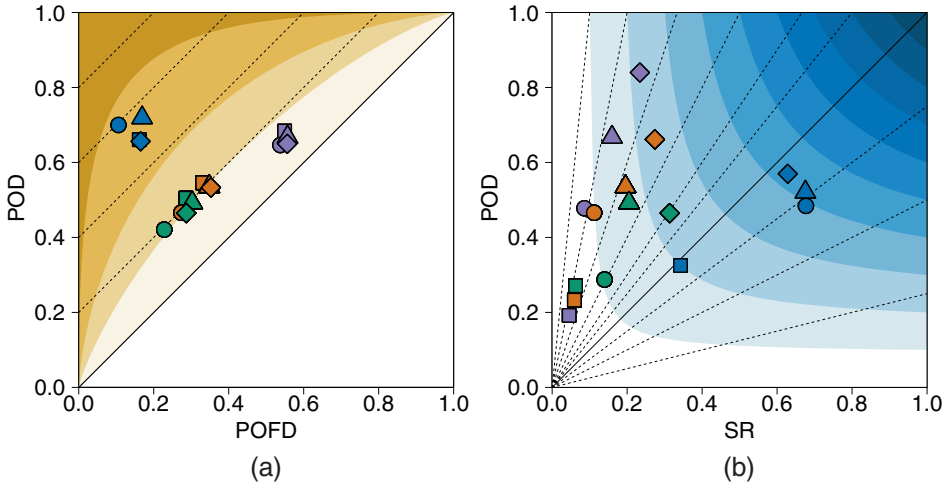


FIGURE 8 As Figure 7, but for the maximum cell area separation with $\chi = 60\,\mathrm{km}^2$. The best predictors of the respective clusters can be read from Supporting Information Tables S3 and S4 (underlined, bold score values). POD, probability of detection; POFD, probability of false detection; SR, success ratio.

importance than ambient variables are, which only show a weak statistical relationship with both targets lifetime T and maximum cell area $A_{\max}$. Nevertheless, most scores indicate a somewhat higher skill for the discrimination of small and large cells for all ambient variable clusters. This is reversed for the dynamical cluster, however, when more extreme lifetime and cell area groups are chosen; for example, with $\tau = 100\,\mathrm{min}$ and $\chi = 80\,\mathrm{km}^2$ (taking into account the equal division of the groups of lifetime and maximum area; not shown). In that case, the separate results for the lifetime and maximum cell area discrimination do not change much qualitatively, and the findings for the predictors can be interpreted similarly to the explanations earlier herein.

4.1.3 | A simple life-cycle model with one ambient variable

Despite the weak statistical relationships of ambient variables and the targets cell lifetime T and maximum cell area $A_{\max}$ discussed earlier herein, a potentially useful approach for the integration of an ambient variable in a simple life-cycle model is presented in this section. As shown in Wapler (2021), the temporal evolution of the mean cell area A can suitably be approximated by a parabola opened downwards. In Appendix A.1, their findings are briefly recapped, and a mathematical parabola formulation is introduced, which the following derivations build upon.

The mathematical parabola model introduced in Equation (A1) (see Appendix A.1) describing this evolution can be refined by adding an ambient variable as second form parameter u. The model then reads as follows:

$$A^{(T,u)}(t) = A^{(T,u)}_{\max} - \frac{A^{(T,u)}_{\max} - A^{(T,u)}_{\min}}{(T/2)^2}\left(t - \frac{T}{2}\right)^2. \qquad (1)$$

Minimum cell area $A^{(T,u)}_{\min}$ can conveniently be assumed to be independent of T and u: $A^{(T,u)}_{\min} = A_0$. The mean wind and vertical wind shear expressed by the MLS, DLS, or one of the SRHs exhibit no clear monotonic statistical relationship to the maximum amplitude $A^{(T,u)}_{\max} - A^{(T,u)}_{\min} \equiv \mathcal{A}^{(T,u)}$, whereas thermodynamical variables like, for example, $\mathrm{LI_{ML}}$, SI, KO index, or $\mathrm{LR_{700–500}}$, can be incorporated via $\mathcal{A}^{(T,u)} = c_A(u)T$ using a linear assumption for $c_A(u)$. Equation (A2) is then transformed into

$$A^{(T,u)}(t) = A_0 + 4c_A(u)t\left(1 - \frac{t}{T}\right). \qquad (2)$$

A linear regression for $\mathrm{LI_{ML}}$ (in kelvin) yields $c_A(\mathrm{LI_{ML}}) \approx (0.351 - 0.020\mathrm{LI_{ML}})\,\mathrm{km}^2\ \cdot\mathrm{min}^{-1}$ with a root-mean-squared error of $\mathrm{RMSE} = 0.03\,\mathrm{km}^2\ \cdot\mathrm{min}^{-1}$, which leads to differences compared with the parabola model without $\mathrm{LI_{ML}}$ information of $\mathcal{O}(10\ \mathrm{km}^2)$ and more for the same lifetime T. Equation (2) leads to an estimate of the maximum cell area, which is given by

$$A^{(T,u)}_{\max} = A(t = T/2) = A_0 + c_A(u)T \qquad (3)$$

and also valid without u-dependence. As an example (called Example 1) without an ambient variable, for $T = 60\,\mathrm{min}$, a maximum area of $A^{(60\ \mathrm{min})}_{\max} \approx 39\,\mathrm{km}^2$ is obtained (see Figure A2a). With dependence on $\mathrm{LI_{ML}}$, one finds with Equation (3) considering the uncertainty in the calculation of the regression coefficient $c_A(\mathrm{LI_{ML}}) \pm 0.03\,\mathrm{km}^2\ \cdot\mathrm{min}^{-1}$ that there are differences worth mentioning (Figure 9a): the mean maximum area is around $10\,\mathrm{km}^2$ larger for high instability (low $\mathrm{LI_{ML}}$ values) compared with stable conditions (high $\mathrm{LI_{ML}}$ values) for the same lifetime T. This difference is larger than the uncertainty arising from the calculation of $c_A(\mathrm{LI_{ML}})$. Moreover, it becomes clear that the original parabola model from Equation (A2) is equivalent to the parabola model from Equation (2) with $u = \mathrm{LI_{ML}} =$

1477870x, 2023, 755, Downloaded from https://rmets.onlinelibrary.wiley.com/doi/10.1002/qj.4505 by Karlsruher Institution F. Technologie, Wiley Online Library on [10/11/2023]. See the Terms and Conditions (https://onlinelibrary.wiley.com/terms-and-conditions) on Wiley Online Library for rules of use; OA articles are governed by the applicable Creative Commons License

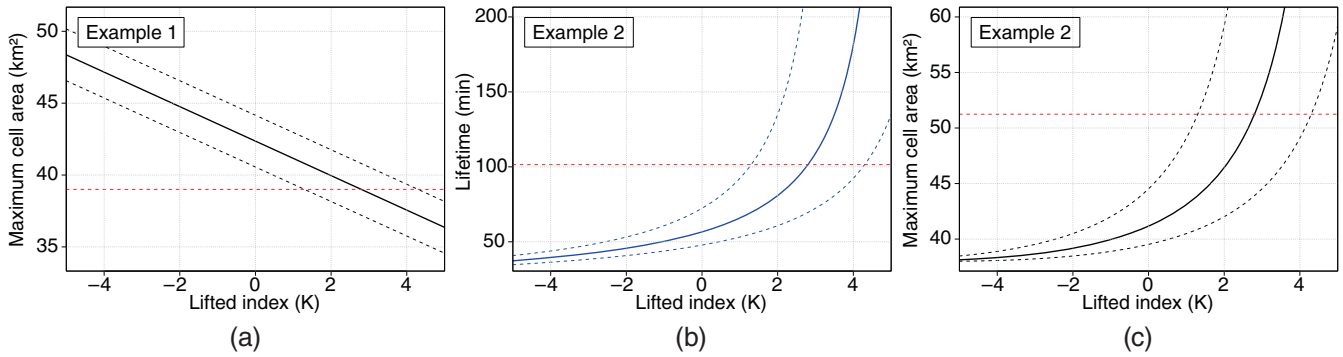


FIGURE 9 (a) Example 1: Maximum cell area A_{max} depending on LI_{ML} as predicted by the parabola model for the example of $T = 60$ min. The solid black line shows the result of Equation (3) for $c_A(LI_{ML}) \approx (0.351 - 0.020LI_{ML})\,km^2 \cdot min^{-1}$; the dashed black lines depict the uncertainty according to the regression RMSE = $0.03\,km^2 \cdot min^{-1}$. The dashed red line gives the result for $c_A = 0.295\,km^2 \cdot min^{-1}$ as obtained for the parabola model without dependence on LI_{ML} (see Appendix A.1). (b) Example 2: Lifetime T depending on LI_{ML} as predicted by the parabola model for the example of $t = 17$ min with $A(t) = 38\,km^2$. The lines are obtained similarly to (a), but using Equation (4). (c) Like (a) but calculated from the lifetime values depicted in (b) of Example 2.

2.8 K, indicating that the maximum cell area is underestimated by the original parabola model in neutral and unstable conditions.

Conversely, solving Equation (2) for T yields estimates for the lifetime T as a function of LI_{ML}, given the cell area $A(t)$ at a specific cell age t:

$$T = \frac{4c_A(u)t^2}{A_0 + 4c_A(u)t - A(t)}. \quad (4)$$

As a second example (called Example 2), one clearly sees for a given cell area $A(t) = 38\,km^2$ at $t = 17$ min (corresponding to the optimal discrimination threshold regarding the maximum cell area A_{max}; see Section 4.1.2) that the lower the LI_{ML} is (i.e., the more unstable the environment is) the shorter is the remaining lifetime and the smaller is the maximum cell area (Figure 9b,c). The interpretation is as follows. For LI_{ML} values in the unstable range of less than 0 K, a cell with $A_{t=17\,min} = 38\,km^2$ has not grown strongly for some reason considering the good thermodynamical conditions. It is therefore expected not to intensify further (i.e., to have a short lifetime and a small maximum area). Another interesting aspect is that the uncertainty ranges substantially increase, when the chosen cell area $A(t)$ approaches the theoretical limit of the parabola model $A_{crit}^{(LI_{ML})}(t) = A_0 + 4c_A(LI_{ML})t$ (see Appendix A.1). Uncertainties arising from other sources, like the inaccuracy of the definition of the cell area or cell age, caused, for example, by shadowing effects in the radar data or the KONRAD cell definition, are, of course, not included in the presented uncertainty ranges.

Separate statistics of cells occurring in rather unstable ($LI_{ML} < -1$ K) and rather stable ($LI_{ML} \geq -1$ K) conditions depict these differences well (Figure 10). As mentioned in the preceding discrimination analysis (Sections 4.1.1 and 4.1.2), values around −1 K are discriminating best between long- and short-living cells, as well as between cells with small and large maximum cell areas in terms of PSS (see Supporting Information Tables S1 and S3). The fraction of long-living cells with $T > 60$ min is 3.4% for unstable conditions and 2.4% for rather stable conditions. The areas of cells occurring in rather unstable conditions grow faster than those for cells occurring in more stable conditions. The lower the LI_{ML} values are the higher is the convective instability, and thus the possibility for rapid growth through free convection. Nevertheless, large overlapping areas remain between the curves of different lifetimes as well as between the high-LI and low-LI curves, representing the large variability of individual cell life cycles. The limited sample size makes the incorporation of more than one ambient variable less confident, as the representativeness of the multivariate regression in the calculation of c_A degrades with higher dimensionality. This deficiency might shrink for longer study periods.

4.2 | Bivariate analyses

Separating the dataset into classes of short- and long-living or small and large cells, as already described in Sections 4.1.1 and 4.1.2, and comparing their PDFs as a function of two ambient variables reveal their combined statistical connections. As in Figure 6, the findings for the cell area $A_{t=7\,min}$, DLS, and LI_{ML}, which represent three different predictor clusters (see Figure 5), are illustrated as examples (Figure 11). The evaluation scores are again summarised in the ROC and performance diagrams (Figure 12). The results are not depicted for all possible bivariate predictor combinations, but only for a selection: all bivariate predictor combinations are considered, where

1477870x, 2023, 755, Downloaded from https://rmets.onlinelibrary.wiley.com/doi/10.1002/qj.4505 by Karlsruher Institution F. Technologie, Wiley Online Library on [10/11/2023]. See the Terms and Conditions (https://onlinelibrary.wiley.com/terms-and-conditions) on Wiley Online Library for rules of use; OA articles are governed by the applicable Creative Commons License

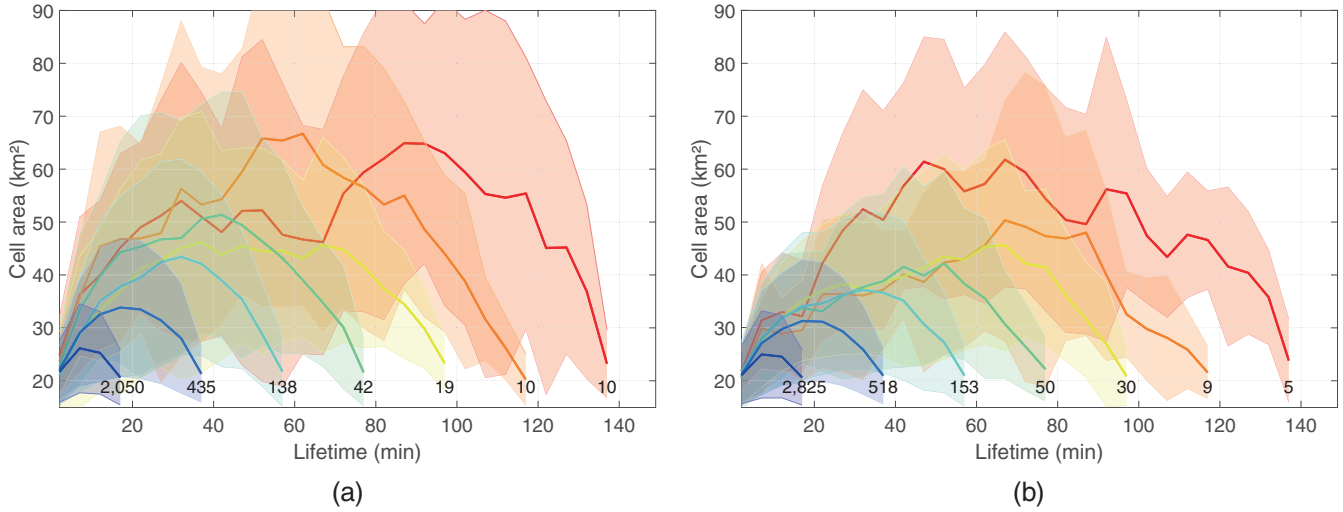


FIGURE 10 As Figure A1b in Appendix A.1, but separated for cells associated with LI_{ML} (a) below or equal to −1 K (N = 16,282) and (b) above −1 K (N = 22,271). Note that only every fourth line is drawn, and that the number of cells for long lifetimes is low.

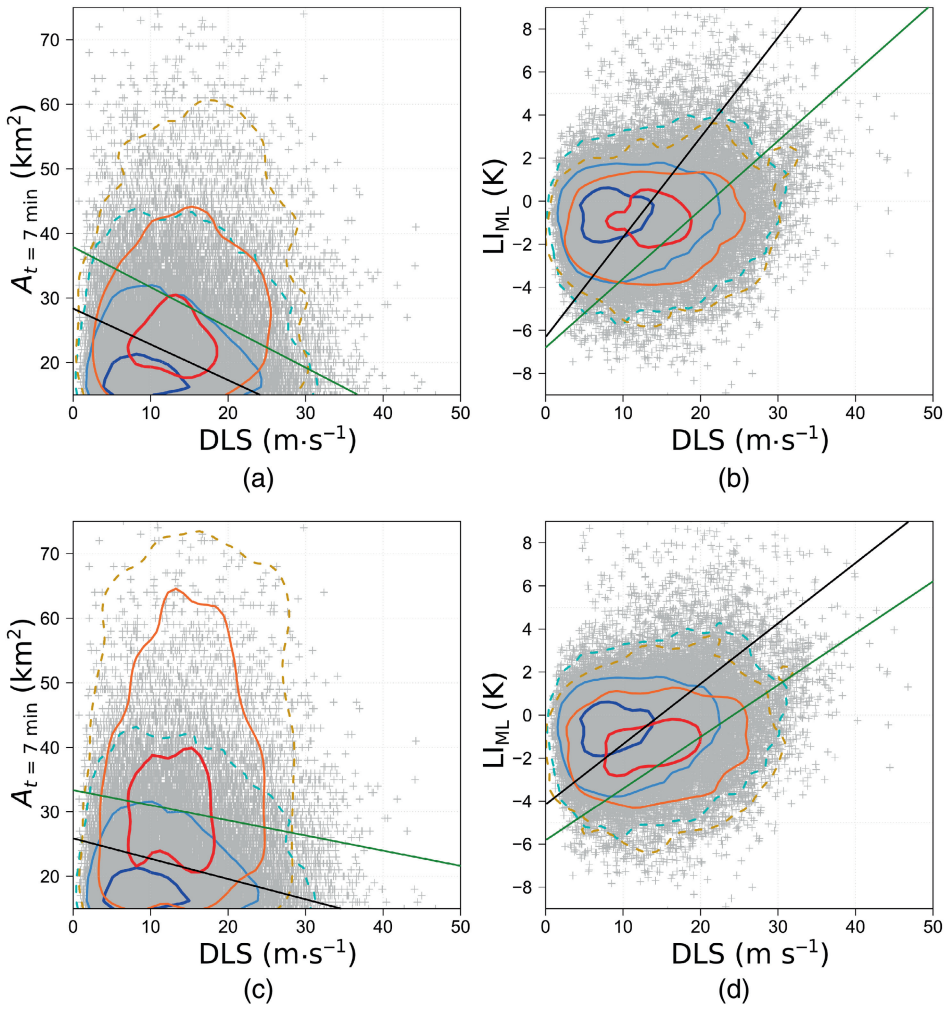


FIGURE 11 Scatter plot of all 38,553 cells and comparison of two-dimensional probability density functions from kernel density estimation for (a, b) cell separation with τ = 60 min in short lifetime (blue hues; N = 37,457) and long lifetime (red hues; N = 1,096), and (c, d) cell separation with χ = 60 km² in small maximum cell area (blue hues; N = 37,443) and large maximum cell area (red hues; N = 1,052), as a function of (a, c) the combination of deep-layer shear (DLS) and cell area $A_{t=7\ min}$, as well as (b, d) DLS and mixed-layer lifted index LI_{ML}. The contour lines indicate the respective 0.25 (solid, red/dark blue), 0.75 (solid, orange/light blue) and 0.95 (dashed) frequency levels; for example, 75% of the long-living or large cells are located within the respective solid orange contour. Similar to Figure 6, the black and green lines indicate the optimal thresholds according to the Peirce skill score and critical success index respectively, based on a linear discriminant analysis.

1477870x, 2023, 755, Downloaded from https://rmets.onlinelibrary.wiley.com/doi/10.1002/qj.4505 by Karlsruher Institution F. Technologie, Wiley Online Library on [10/11/2023]. See the Terms and Conditions (https://onlinelibrary.wiley.com/terms-and-conditions) on Wiley Online Library for rules of use; OA articles are governed by the applicable Creative Commons License

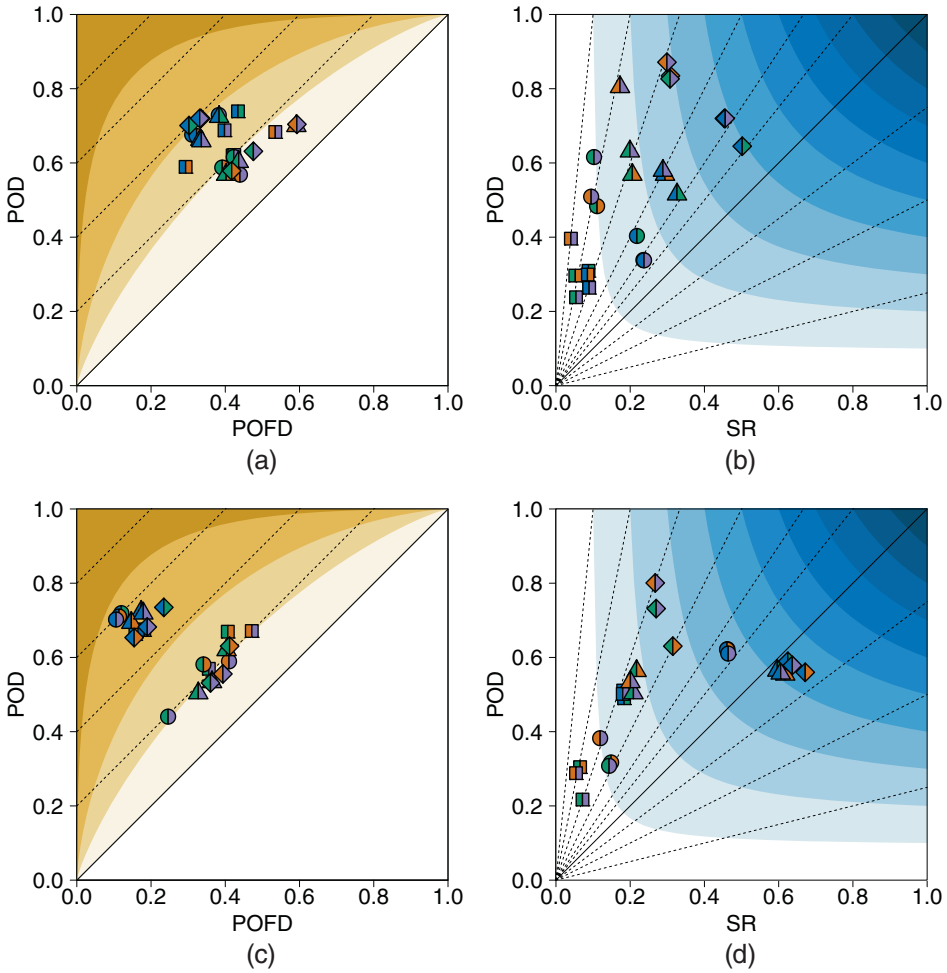


FIGURE 12 Similar to Figures 7 and 8 but for the best combinations of two predictors from the four variable clusters in Figure 5. The marker fill shows the respective two colours according to the cluster combination. (a, b) Lifetime estimation; (c, d) maximum cell area estimation. POD, probability of detection; POFD, probability of false detection; SR, success ratio.

the predictors originate from two different clusters. From these predictor combinations, only those are drawn that reach the highest PSS and CSI for their respective specific cluster combination. This is done independently for all four different prediction times. Similar to the univariate procedure described in Section 4.1.1 for the determination of the optimal variable threshold, thresholding lines in the 2D variable spaces have optimally been calculated in an iterative procedure with 100 repetitions, here by means of a linear discriminant analysis.

The cell area $A_{t=7\ \mathrm{min}}$ and DLS as predictors have a combined discrimination skill that is mirrored by a shift in the dense core area of the 2D PDFs from kernel density estimation toward higher cell area and DLS values for the long-living and large cell group respectively (Figure 11a,c). Compared with the univariate score values of A, the combination with DLS leads only to a minor improvement for the lifetime estimation. Depending on the prediction time point, PSS increases only by 0.01 to 0.02, and CSI increases by 0.01 at most (not shown). For the estimation of A_{max}, these metrics are not improved. The combination of A and DLS reaches scores very close to the best variable combinations from the cell (core) cluster and the dynamical cluster.

In general, when comparing Figure 7 with Figure 12a,b and Figure 8 with Figure 12c,d, it is apparent that the bivariate scores are not much better than the univariate scores are. The greatest improvements can be seen for combinations of variables from two ambient variable clusters. As an example, the combination of DLS and $\mathrm{LI}_{\mathrm{ML}}$ (see also Figure 11b,d) is in many cases the best ambient variable combination (or very close to it): for the lifetime estimation, the PSS increases by up to 0.03, and the CSI increases by up to 0.01. For the maximum cell area estimation, the highest increases are by 0.10 for the PSS and by 0.04 for the CSI. However, combinations of any ambient variable cluster with the cell (core) cluster achieve the highest skill. Combinations of two clusters seem to improve the biases in many cases compared with the univariate values. As a last note, the optimal thresholding lines for PSS divide the high-frequency regions of the PDFs (areas within the solid blue and red lines in Figure 11) well, whereas the lines for CSI are located at predictor values that are more favourable for a long cell lifetime and a large maximum area (similar to the univariate case; see Figure 6). For these thresholding lines, the number of missed events is as high as or even higher than the number of hits.

1477870x, 2023, 755, Downloaded from https://rmets.onlinelibrary.wiley.com/doi/10.1002/qj.4505 by Karlsruher Institution F. Technologie, Wiley Online Library on [10/11/2023]. See the Terms and Conditions (https://onlinelibrary.wiley.com/terms-and-conditions) on Wiley Online Library for rules of use; OA articles are governed by the applicable Creative Commons License

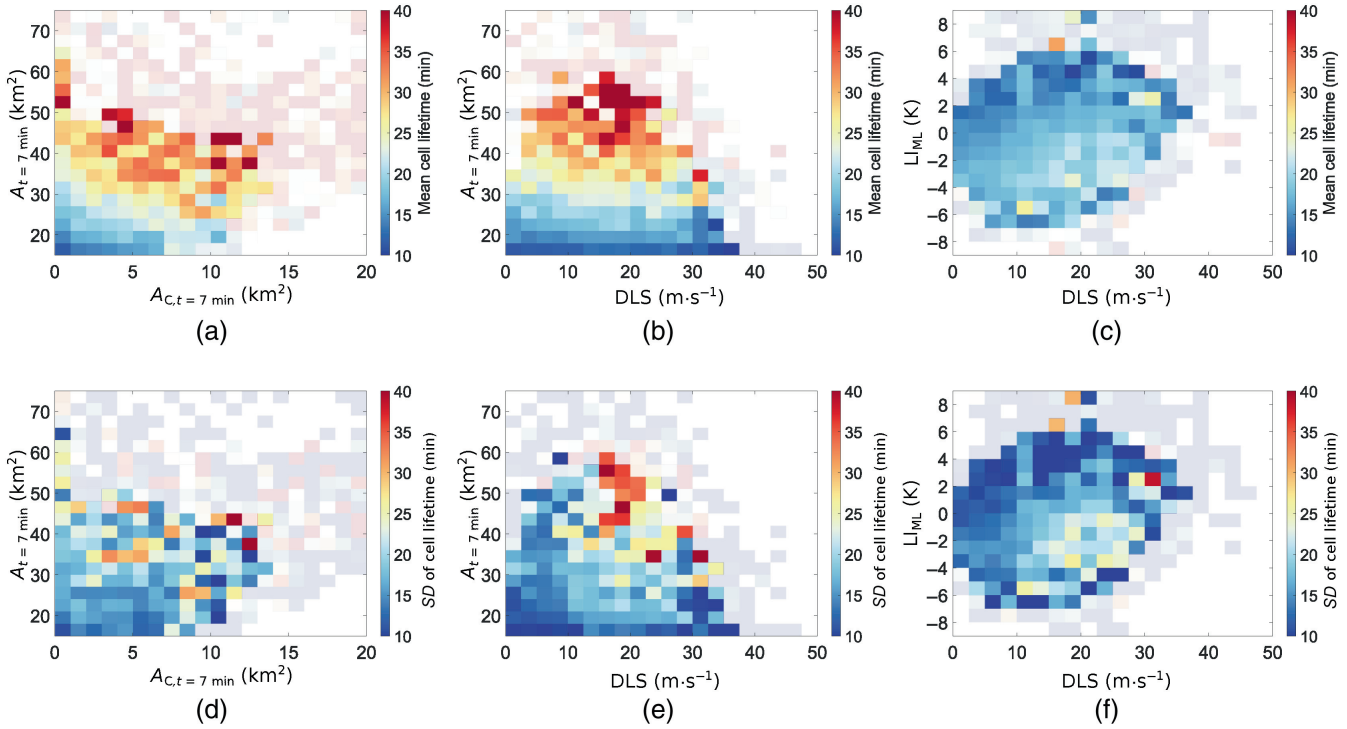


FIGURE 13 (a)–(c) Mean lifetime of all 38,553 cells, as a function of the combination of (a) core area $A_{C,t=7\ min}$ and cell area $A_{t=7\ min}$, (b) deep-layer shear (DLS) and cell area $A_{t=7\ min}$, and (c) DLS and mixed-layer lifted index LI_{ML}. The predictor values are each grouped in 20 intervals. Groups containing fewer than 10 cells are shown transparently. (d)–(f) The respective standard deviations (*SD*) in the same manner.

As could be expected from the previous analyses, the mean lifetime increases with increasing vertical wind shear and instability, as well as with increasing cell and core area after 7 min. The mean lifetime differences between different predictor ranges are higher for predictor combinations with the cell area A (25–30 min; Figure 13a,b) than for combinations of ambient variables solely (10–15 min; Figure 13c; Figure A4). These differences are higher than those for grouping by only one of the ambient variables, leading to a difference of at most 7–10 min (not shown). The standard deviations (Figure 13d–f) are approximately of the same order as the mean lifetime differences, meaning that the latter should be interpreted carefully. The high standard deviations originate, inter alia, from the fact that, on days with convection-favouring conditions, not only do long-living cells develop but also many short-living cells (see Figure 2b).

Very similar results apply qualitatively to the maximum cell area differences and respective standard deviations, albeit the relative differences of the maximum cell area are somewhat higher (Figure 14). The mean maximum area increases from around 20 km^2 for weak initial cell growth to more than 50 km^2 for strong initial growth (Figure 14a). The cell growth is more decisive for the maximum area than DLS is (Figure 14b). High vertical wind shear, however, combined with convective instability procures a maximum area of around 35 km^2, whereas cells grow only slightly (up to around 20–25 km^2) during stable conditions with little shear (Figure 14c).

When considering only cells that reached a lifetime of at least 30 min, the mean lifetime and maximum area increase for the groups that are conducive for longer lifetimes/larger areas owing to the larger relative frequency of the long-living and large cells in these groups. For example, at high DLS (>15 m·s^{-1}) and low LI_{ML} (less than −1 K) values, the lifetime is expected to be around 55–60 min, and the maximum area is expected to be around 55–60 km^2, which is 20–25 min longer and 20–25 km^2 larger than at low DLS and high LI_{ML} values (not shown). Thus, the lifetime and maximum area differences between different predictor groups increase when short-living cells with a lifetime of less than 30 min are not taken into account for the evaluation. This is in line with the increased forecast performance in terms of CSI for later prediction times in the categorical analyses earlier herein.

The investigations of combined dependencies with even more than two predictors hardly show groups with sufficient large sample sizes for establishing robust statistical relations (not shown). A clear relationship could

1477870x, 2023, 755, Downloaded from https://rmets.onlinelibrary.wiley.com/doi/10.1002/qj.4505 by Karlsruher Institution F. Technologie, Wiley Online Library on [10/11/2023]. See the Terms and Conditions (https://onlinelibrary.wiley.com/terms-and-conditions) on Wiley Online Library for rules of use; OA articles are governed by the applicable Creative Commons License

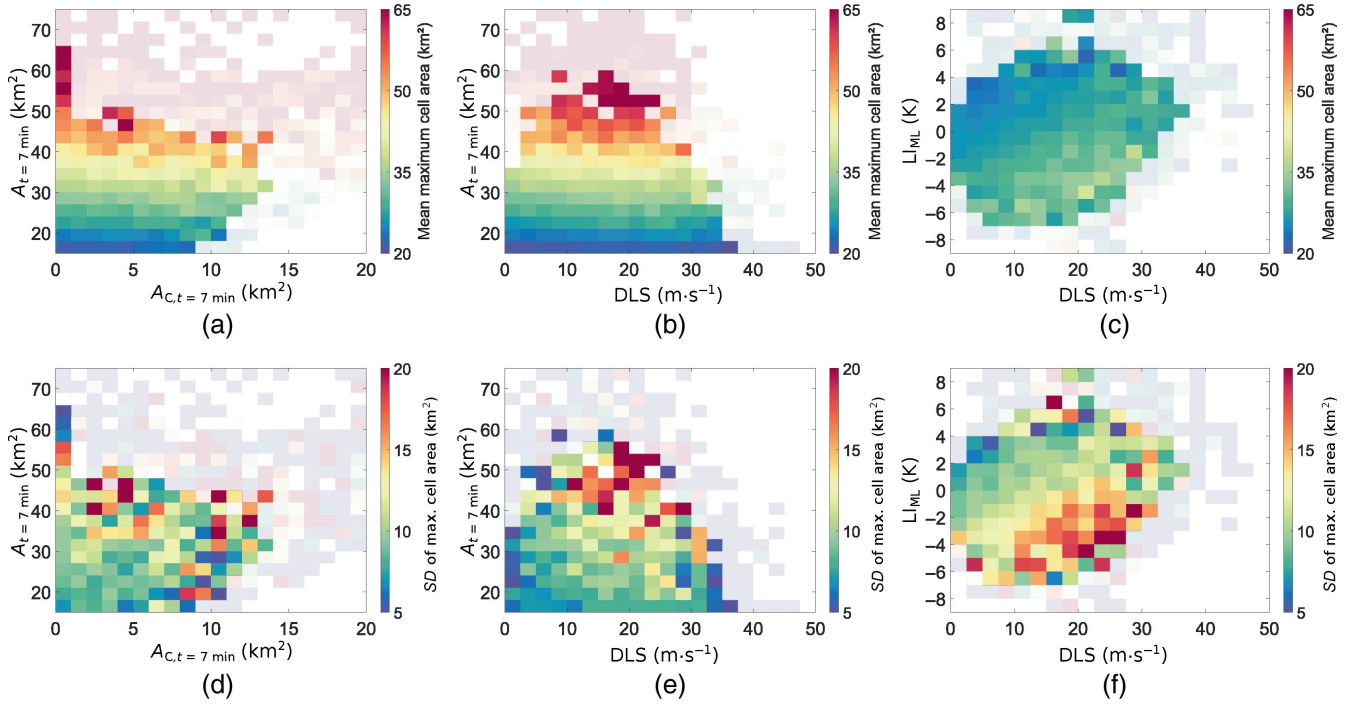


FIGURE 14 Like Figure 13 but for the mean and standard deviations (*SD*) of maximum cell area instead of lifetime. Note the different colour bar ranges.

not be extracted due to the existence of too many uncovered subspaces in the multidimensional space. Advanced statistical and machine-learning methods offer ways in which to achieve a potentially better predictive skill in the future by using more than two predictors simultaneously. They also provide the possibility of quantifying the particular importance of the predictors for life-cycle estimations and of addressing the corresponding uncertainties for nowcasting applications.

5 | SUMMARY AND CONCLUSIONS

The life cycles of convective storms in Germany are analysed taking into account the prevailing atmospheric ambient conditions by means of a unique object-based dataset. This dataset combines cell objects derived from DWD's cell detection and tracking algorithm, KONRAD, with high-resolution NWP assimilation analysis fields of COSMO-EU. The focus of the study is on isolated convection, which passed through an undisturbed life cycle without any impact of another convective cell in its vicinity, so cell clusters and several supercells have been filtered out. The general research questions are which multivariate statistical correlations exist between different variables describing the prevailing ambient conditions of convective cells, and which of these variables and which cell attributes exhibit statistical relationships to life-cycle attributes such as storm lifetime T and maximum horizontal extent A_{max}. These analyses provide the basis for further investigations on how the data and findings can be used to develop statistical or machine-learning models that provide life-cycle estimations, with the objective to improve automated multidata real-time nowcasting procedures.

Taking up the main research questions posed in Section 1, our conclusions are as follows.

(1) Under which range of prevailing ambient conditions does DMC develop, and how are the related ambient variables statistically correlated with each other and with cell attributes at the beginning of the cells' life cycle?

(a) Most of the isolated convective cells occurred in rather calm to moderate dynamical conditions, associated with some convective instability and moderate to high moisture amounts.
(b) A clustering, which bundles highly correlated variables in separate clusters, reveals one dynamical cluster, representing the midtropospheric flow and vertical shear (e.g., U_{3-6}, SRH_{0-3}, DLS), as well as two clusters consisting of thermodynamical and moisture quantities. Of the latter, the first cluster represents convective instability in the middle troposphere (e.g., $LR_{700-500}$, RH_{700}), whereas the second one consists of a collection of variables

1477870x, 2023, 755, Downloaded from https://rmets.onlinelibrary.wiley.com/doi/10.1002/qj.4505 by Karlsruher Institution F. Technologie, Wiley Online Library on [10/11/2023]. See the Terms and Conditions (https://onlinelibrary.wiley.com/terms-and-conditions) on Wiley Online Library for rules of use; OA articles are governed by the applicable Creative Commons License

describing air mass temperature (e.g., T_{850}, $h_{0°C}$) and moisture (e.g., IWV), and of further convective instability indices (e.g., LI_{ML}, $CAPE_{MU}$).

(c) When the horizontal cell area A ($Z \geq 46$ dBZ) and core area A_C ($Z \geq 55$ dBZ), their ratio, and the cell propagation speed c, as observed 5 min after the first cell detection, are included in the cluster analysis, the latter joins the dynamical cluster, while the cell (core) area variables form a separate fourth cluster.

(d) Correlations between variables within the clusters can be very strong – for example, between $CAPE_{MU}$ and LI_{ML}, and between DLS and $U_{3–6}$ – showing that the former is mainly determined by the midtropospheric wind. Cross-cluster correlations are generally mostly weak, but some reach values up to $|r_S| = 0.52$, like the correlation between IWV and $LR_{700–500}$.

(2) Which ambient variables and cell attributes correlate best with the storm properties lifetime and maximum area, indicating the potential for the improvement of nowcasting procedures?

(a) In general, the statistical relevance of ambient variables for the cells' lifetime and maximum area is rather low.

(b) The discrimination skill between short- and long-living cells is higher for dynamical variables than for the other two ambient variable clusters, presumably due to their influence on the degree of cell organisation.

(c) The discrimination skill between cells with small and large maximum cell area is similar for dynamical and thermodynamical variables, and it is slightly higher than the skill for the cell lifetime discrimination is.

(d) The cell and core area 5–35 min after the first cell detection show a (much) higher skill for discriminating between cells with short and long lifetimes or small and large maximum areas. Thus, the cell history is more important than ambient variables are.

(e) The highest univariate skill can be reported for the discrimination of the maximum cell area based on the cell (core) cluster (i.e., without any knowledge about the ambient conditions), particularly for the cell area 5–35 min after the first cell detection representing the initial growth of the cells.

(f) The bivariate skill for combinations of variables from two different clusters does not increase much, when the cell (core) area is combined with an ambient variable, but it is the highest among all combinations. The mean lifetime is 25-30 min higher, and the mean maximum area is more than 30 km^2 larger for high wind shear and a large cell area 5 min after the first cell detection than for weak wind shear and a small cell area.

(g) The bivariate skill for combinations from two ambient variable clusters can be higher than the univariate skill is; for example, for the combination of DLS and LI_{ML}. The mean differences between high-shear low-LI and low-shear high-LI conditions are 10–15 min for the lifetime and 10–15 km^2 for the maximum cell area. The information about the ambient variables makes it possible to estimate the storm lifetime and the maximum area at least with some skill even before cells develop in the respective environments.

As presented by Wapler (2021), an axially symmetric parabola opened downwards describes the mean cell area evolution well. The study at hand revealed that this model has second-order limitations, as the timing of the maximum cell area shifts to later life-cycle stages with increasing lifetime. However, an advantage is that the parabola model can be easily refined by adding one ambient variable as a form parameter. Utilising, for example, LI_{ML}, the analyses show that, for higher instability, the mean parabola curves are somewhat steeper and thus represent a faster growth during the first 15–30 min of the life cycle. Estimates for the maximum cell area and the lifetime with this refined model differ noticeably depending on instability. Still, the individual life cycles show high variability, and considerable uncertainties remain in these estimates stemming from the parameter calculation for the statistical regression model, as well as the inaccuracy of the definition of the cell area or cell age, caused, for example, by shadowing effects in the radar data or the KONRAD cell definition. An alternative, non-parametric approach to the parametric parabola model with a different perspective on cell life cycles, where cell evolution is represented by a flow field in a feature space, seems to be worth investigating in the context of probabilistic nowcasting procedures in the future.

The limitations of the lifetime or cell area discrimination and the corresponding differences of the mean values for specific ambient conditions, described in the last list item, may have several reasons. First, even if the mesoscale conditions as identified by model analyses appear very similar, the actual storm development characteristics can look very different depending on the trigger mechanisms and non-resolved local- or microscale processes (e.g., orographic features, low-level convergence, cloud processes). On days with similar widespread convection-favouring conditions, a high number of short-living and small cells may still occur (see Section 3.1), and only a few of these

1477870x, 2023, 755, Downloaded from https://rmets.onlinelibrary.wiley.com/doi/10.1002/qj.4505 by Karlsruher Institution F. Technologie, Wiley Online Library on [10/11/2023]. See the Terms and Conditions (https://onlinelibrary.wiley.com/terms-and-conditions) on Wiley Online Library for rules of use; OA articles are governed by the applicable Creative Commons License

cells may develop into long-living and large cells. Second, as described in Section 2.3, the ambient variables from COSMO-EU were attributed to the KONRAD cells such that single statistical measures or numbers represent the cells' environment conditions. What was not considered in the methods of this study are the mesoscale gradients around the position of the convective cells, which may give more information than the projection of the ambient variables onto the cell objects does. Third, the strict detection criterion and the tracking method of KONRAD cut off considerable parts of the cumulus and the dissipation stage of the cells. Moreover, a cell not fulfilling the detection criterion for one time instance during its real life cycle is split into two individual KONRAD cells. Fourth, only uni- and bivariate relations between the predictors (ambient variables and some cell attributes at the initial stage) and life-cycle properties T and $A_{\max}$ were presented. Similar investigations of combined dependencies with even more than two ambient variables, however, hardly reveal combinations with a sufficiently large sample size for establishing robust statistical relations and, at the same time, remarkably stronger signals with regard to the mean lifetime or mean maximum area (Wilhelm, 2022). Fifth, the ambient conditions are characterised by high-resolution model analysis data, which are a very good approximation but do not completely reflect the actual reality. Sixth, owing to the different scales and processes involved, the chaotic behaviour of the atmosphere strongly affects the challenges listed herein.

For studying the potential additional benefit of considering more than two variables, for quantifying their particular importance for life-cycle estimations, and for addressing the corresponding uncertainties, advanced statistical or machine-learning methods have great potential to be successfully applied to the data (Ukkonen and Mäkelä, 2019; Mecikalski *et al.,* 2021). The adaptation of the methods used by Sherburn *et al.* (2016) or Kunz *et al.* (2020), taking into account the spatial distribution of ambient variables, may provide more insights into the mesoscale processes involved and unravel more complex relations to storm properties, such as cell lifetime or maximum area. Beyond that, applying (convolutional) neural networks as a machine-learning-based approach might be beneficial for identifying such complex relations and the relative importance of the variable fields (Kamangir *et al.,* 2020; Molina *et al.,* 2021).

In terms of a multisensor/multidata approach (e.g., Nisi *et al.,* 2014; James *et al.,* 2018; Cintineo *et al.,* 2020; Zöbisch *et al.,* 2020), a combination of the existing dataset of this study with further data derived by radar, satellite, or lightning detection measurements could enhance the multidimensional picture of the measurable properties of convective cells. Advances in the cell detection and tracking algorithms as, for example, the currently pre-operational algorithm KONRAD3D of the DWD (Werner, 2020), relying on 3D radar reflectivity, will be able to describe the life cycles of convective cells more realistically and with a large variety of cell attributes. In addition to the basic information gathered via a 2D-algorithm like KONRAD, such advancements will provide information about the vertical structure and the liquid water content of the cells. Furthermore, information obtained with modern dual-polarisation Doppler radar can be used for hydrometeor classification (e.g., Ryzhkov *et al.,* 2005; Kumjian and Ryzhkov, 2008; Josipovic, 2020) or the automatic detection of mesocyclones (e.g., Hengstebeck *et al.,* 2018; Wapler, 2021). Data from lightning detection yields further valuable information about convective storms (e.g., Farnell *et al.,* 2017; Wapler, 2017). This opens up a large space of further possibilities for statistical life-cycle analyses once a sufficiently large sample of 3D cell objects has been generated.

AUTHOR CONTRIBUTIONS

Jannik Wilhelm: data curation; formal analysis; investigation; methodology; software; validation; visualization; writing – original draft. **Kathrin Wapler:** conceptualization; data curation; methodology; supervision. **Ulrich Blahak:** conceptualization; funding acquisition; methodology; resources; software; supervision. **Roland Potthast:** conceptualization; methodology; resources; software; supervision. **Michael Kunz:** conceptualization; funding acquisition; methodology; project administration; resources; supervision.

ACKNOWLEDGEMENTS

We thank the German Federal Agency for Cartography and Geodesy (Bundesamt für Kartographie und Geodäsie, BKG) as well as Natural Earth for making the use of geodata possible. Jannik Wilhelm appreciates the vivid exchange of ideas with DWD's SINFONY project, especially with Robert Feger, Martin Rempel, and Christian Welzbacher, as well as the very helpful comments of Robert Feger on the manuscript draft. Funding was received from the Federal Ministry for Transport and Digital Infrastructure (BMV; administrative number Z30/SeV/288.3/1582/LF16). We thank the anonymous reviewer and Agostino Manzato for their reasoned and helpful feedback on the manuscript. Open Access funding enabled and organized by Projekt DEAL.

CONFLICT OF INTEREST STATEMENT

The authors declare that they have no conflict of interest.

1477870x, 2023, 755, Downloaded from https://rmets.onlinelibrary.wiley.com/doi/10.1002/qj.4505 by Karlsruher Institution F. Technologie, Wiley Online Library on [10/11/2023]. See the Terms and Conditions (https://onlinelibrary.wiley.com/terms-and-conditions) on Wiley Online Library for rules of use; OA articles are governed by the applicable Creative Commons License

DATA AVAILABILITY STATEMENT

Raw data were generated at the DWD. Derived data supporting the findings of this study are available from the corresponding author (JW) upon request.

ORCID

Jannik Wilhelm https://orcid.org/0000-0002-7475-0758
Michael Kunz https://orcid.org/0000-0002-0202-9558

REFERENCES

Aregger, M.P. (2021) *Stationary and slow-moving convection over Switzerland: A 14-year radar-based climatology*. Master's Thesis, Bern, Faculty of Sciences, University of Bern. https://occrdata.unibe.ch/students/theses/msc/326.pdf [Accessed 22nd March 2023].

Atkins, N.T. and Wakimoto, R.M. (1991) Wet microburst activity over the southeastern United States: implications for forecasting. *Weather and Forecasting*, 6, 470–482.

Bjerknes, J. (1938) Saturated-adiabatic ascent of air through dry-adiabatically descending environment. *Quarterly Journal of the Royal Meteorological Society*, 64, 325–330.

Bolton, D. (1980) The computation of equivalent potential temperature. *Monthly Weather Review*, 108, 1046–1053.

Bronstert, A., Agarwal, A., Bossenkool, B., Peter, M., Heistermann, M., Köhn-Reich, L., Moran, T. and Wendi, D. (2017) Die Sturzflut von Braunsbach am 29. Mai 2016 - Entstehung, Ablauf und Schäden eines "Jahrhundertereignisses". Teil 1: Meteorologische und hydrologische analyse. *Hydrologie und Wasserbewirtschaftung*, 61, 150–162 (in Germany only).

Brooks, H.E. (2007) Ingredients-based forecasting. In: Giaiotti, D.B., Steinacker, R. and Stel, F. (Eds.) *Atmospheric Convection: Research and Operational Forecasting Aspects*. Springer: Vienna, pp. 133–140.

Brooks, H.E. (2009) Proximity soundings for severe convection for Europe and the United States from reanalysis data. *Atmospheric Research*, 93, 546–553.

Brooks, H.E. and Correia, J. (2018) Long-term performance metrics for National Weather Service Tornado Warnings. *Weather and Forecasting*, 33, 1501–1511.

Brooks, H.E., Lee, J.W. and Craven, J.P. (2003) The spatial distribution of severe thunderstorm and tornado environments from global reanalysis data. *Atmospheric Research*, 67-68, 73–94.

Bunkers, M.J., Klimowski, B.A., Zeitler, J.W., Thompson, R.L. and Weisman, M.L. (2000) Predicting supercell motion using a new hodograph technique. *Weather and Forecasting*, 15, 61–79.

Cintineo, J.L., Pavolonis, M.J., Sieglaff, J.M., Cronce, L. and Brunner, J. (2020) NOAA ProbSevere v2.0 – ProbHail, ProbWind, and ProbTor. *Weather and Forecasting*, 35, 1523–1543.

Czernecki, B., Taszarek, M., Marosz, M., Półrolniczak, M., Kolendowicz, L., Wyszogrodzki, A. and Szturc, J. (2019) Application of machine learning to large hail prediction - the importance of radar reflectivity, lightning occurrence and convective parameters derived from ERA5. *Atmospheric Research*, 227, 249–262.

Davini, P., Bechini, R., Cremonini, R. and Cassardo, C. (2012) Radar-based analysis of convective storms over northwestern Italy. *Atmosphere*, 3, 33–58.

Doswell, C.A. (1987) The distinction between large-scale and mesoscale contribution to severe convection: a case study example. *Weather and Forecasting*, 2, 3–16.

DWD. (2014) *Assimilation von Radar-Niederschlagdaten Im COSMO-EU (in German only)*. Offenbach: Deutscher Wetterdienst. https://www.dwd.de/DE/fachnutzer/forschung_lehre/numerische_wettervorhersage/nwv_aenderungen/_functions/DownloadBox_modellaenderungen/cosmo_eu/pdf_2011_2015/pdf_lme_03_09_2014.pdf?__blob=publicationFile&v=7 [Accessed 22nd March 2023].

Farnell, C., Rigo, T. and Pineda, N. (2017) Lightning jump as a nowcast predictor: application to severe weather events in Catalonia. *Atmospheric Research*, 183, 130–141.

Feger, R., Werner, M., Posada, R., Wapler, K. and Blahak, U. (2019) Generation of an object-based nowcasting ensemble. In: *3rd European Nowcasting Conference*. Madrid: Agencia Estatal de Meteorología. http://hdl.handle.net/20.500.11765/10631 [Accessed 22nd March 2023].

Fluck, E. (2018) *Hail statistics for European countries*. Ph.D. Thesis, Karlsruhe, Karlsruhe Institute of Technology (KIT). https://doi.org/10.5445/IR/1000080663 [Accessed 22nd March 2023].

Gensini, V.A. and Tippett, M.K. (2019) Global ensemble forecast system (GEFS) predictions of days 1-15 U.S. tornado and hail frequencies. *Geophysical Research Letters*, 46, 2922–2930.

Goudenhoofdt, E. and Delobbe, L. (2013) Statistical characteristics of convective storms in Belgium derived from volumetric weather radar observations. *Journal of Applied Meteorology and Climatology*, 52, 918–934.

Haklander, A.J. and van Delden, A. (2003) Thunderstorm predictors and their forecast skill for the Netherlands. *Atmospheric Research*, 67-68, 273–299.

Hamann, U., Zeder, J., Beusch, L., Clementi, L., Foresti, L., Hering, A., Nerini, D., Nisi, L., Sassi, M. and Germann, U. (2019) Nowcasting of thunderstorm severity with machine learning in the Alpine region. In: *3rd European Nowcasting Conference*. Madrid: Agencia Estatal de Meteorología. https://repositorio.aemet.es/handle/20.500.11765/10617 [Accessed 22nd March 2023].

Hengstebeck, T., Wapler, K., Heizenreder, D. and Joe, P. (2018) Radar network-based detection of mesocyclones at the German weather service. *Journal of Atmospheric and Oceanic Technology*, 35, 299–321.

Holton, J.R. (2004) *An Introduction to Dynamic Meteorology*. *International Geophysics Series*. London: Elsevier Academic Press.

Hübl, J. (2017) Hochwasser Simbach 2016: Dokumentation und analyse. In: Heimerl, S. (Ed.) *Vorsorgender Und Nachsorgender Hochwasserschutz (in German only)*. Springer: Wiesbaden, pp. 139–150.

Huntrieser, H., Schiesser, H.-H., Schmid, W. and Waldvogel, A. (1997) Comparison of traditional and newly developed thunderstorm indices for Switzerland. *Weather and Forecasting*, 12, 108–125.

James, P.M., Reichert, B.K. and Heizenreder, D. (2018) NowCastMIX: automatic integrated warnings for severe convection on nowcasting time scales at the German weather service. *Weather and Forecasting*, 33, 1413–1433.

Johns, R.H. and Doswell, C.A. (1992) Severe local storms forecasting. *Weather and Forecasting*, 7, 588–612.

Josipovic, L. (2020) *Interaction of three-dimensional properties in the convective cell development*. Master's Thesis, Institute for

1477870x, 2023, 755, Downloaded from https://rmets.onlinelibrary.wiley.com/doi/10.1002/qj.4505 by Karlsruher Institution F. Technologie, Wiley Online Library on [10/11/2023]. See the Terms and Conditions (https://onlinelibrary.wiley.com/terms-and-conditions) on Wiley Online Library for rules of use; OA articles are governed by the applicable Creative Commons License

Atmospheric and Environmental Sciences, Goethe University Frankfurt am Main (Personal communication).

Kaltenböck, R., Diendorfer, G. and Dotzek, N. (2009) Evaluation of thunderstorm indices from ECMWF analyses, lightning data and severe storm reports. *Atmospheric Research*, 93, 381–396.

Kamangir, H., Collins, W., Tissot, P. and King, S.A. (2020) A deep-learning model to predict thunderstorms within 400 km^2 South Texas domains. *Meteorological Applications*, 27, e1905.

Kapsch, M.-L., Kunz, M., Vitolo, R. and Economou, T. (2012) Long-term trends of hail-related weather types in an ensemble of regional climate models using a Bayesian approach. *Journal of Geophysical Research: Atmospheres*, 117, D15107.

Kaufman, L. and Rousseeuw, P.J. (1990) *Finding Groups in Data: An Introduction to Cluster Analysis*. New York: John Wiley & Sons.

Kumjian, M.R. and Ryzhkov, A.V. (2008) Polarimetric signatures in supercell thunderstorms. *Journal of Applied Meteorology and Climatology*, 47, 1940–1961.

Kunz, M. (2007) The skill of convective parameters and indices to predict isolated and severe thunderstorms. *Natural Hazards and Earth System Sciences*, 7, 327–342.

Kunz, M., Blahak, U., Handwerker, J., Schmidberger, M., Punge, H.J., Mohr, S., Fluck, E. and Bedka, K.M. (2018) The severe hailstorm in Southwest Germany on 28 July 2013: characteristics, impacts and meteorological conditions. *Quarterly Journal of the Royal Meteorological Society*, 144, 231–250.

Kunz, M., Wandel, J., Fluck, E., Baumstark, S., Mohr, S. and Schemm, S. (2020) Ambient conditions prevailing during hail events in Central Europe. *Natural Hazards and Earth System Sciences*, 20, 1867–1887.

Lang, P. (2001) Cell tracking and warning indicators derived from operational radar products. In: *Proceedings of the 30th International Conference on Radar Meteorology (Munich)*. Boston, MA: American Meteorological Society, pp. 245–247.

Lang, P., Plörer, P., Munier, H. and Riedl, J. (2003) *KONRAD: Konvektionsentwicklung in Radarprodukte—ein operationelles Verfahren zur analyse von Gewitterzellen und deren Zugbahnen, basierend auf Wetterradarprodukten (in German only)*. Technical Report. Berichte des Deutschen Wetterdienstes 222, Selbstverlag des Deutschen Wetterdienstes, Deutscher Wetterdienst, Offenbach.

Lee, J.W. (2002) *Tornado proximity soundings from the NCEP/NCAR reanalysis data*. Master's Thesis, Norman, OK, School of Meteorology, University of Oklahoma. https://hdl.handle.net/11244/330720 [Accessed 22nd March 2023].

Lloyd, S.P. (1982) Least squares quantization in PCM. *IEEE Transactions on Information Theory*, 28, 129–137.

MacQueen, J. (1967) Some methods for classification and analysis of multivariate observations. In: Le Cam, L.M. and Neyman, J. (Eds.) *Proceedings of the 5th Berkeley Symposium on Mathematical Statistics and Probability*. Berkeley, CA: University of California Press, pp. 281–297.

Mammen, T., Lange, B., Frech, M. and Desler, K. (2010) 3rd generation of systems in the DWD weather radar network. 6th European Conference on Radar in Meteorology and Hydrology. 6-10. Sibiu (Personal communication).

Manzato, A. (2003) A climatology of instability indices derived from Friuli Venezia Giulia soundings, using three different methods. *Atmospheric Research*, 67–68, 417–454.

Manzato, A. (2007) A note on the maximum Peirce skill score. *Weather and Forecasting*, 22, 1148–1154.

Manzato, A. (2012) Hail in Northeast Italy: climatology and bivariate analysis with the sounding-derived indices. *Journal of Applied Meteorology and Climatology*, 51, 449–467.

Markowski, P. and Richardson, Y. (2010) *Mesoscale Meteorology in Midlatitudes*. Chichester: John Wiley & Sons.

Mason, I. (1982) A model for assessment of weather forecasts. *Australian Meteorological Magazine*, 30, 291–303.

Mecikalski, J.R., Sandmæl, T.N., Murillo, E.M., Homeyer, C.R., Bedka, K.M., Apke, J.M. and Jewett, C.P. (2021) A random-forest model to assess predictor importance and nowcast severe storms using high-resolution radar-GOES satellite-lightning observations. *Monthly Weather Review*, 149, 1725–1746.

Miller, P.W. and Mote, T.L. (2018) Characterizing severe weather potential in synoptically weakly forced thunderstorm environments. *Natural Hazards and Earth System Sciences*, 18, 1261–1277.

Mohr, S. and Kunz, M. (2013) Recent trends and variabilities of convective parameters relevant for hail events in Germany and Europe. *Atmospheric Research*, 123, 213–228.

Mohr, S., Wandel, J., Lenggenhager, S. and Martius, O. (2019) Relationship between atmospheric blocking and warm-season thunderstorms over western and Central Europe. *Quarterly Journal of the Royal Meteorological Society*, 145, 3040–3056.

Mohr, S., Wilhelm, J., Wandel, J., Kunz, M., Portmann, R., Punge, H.J., Schmidberger, M., Quinting, J.F. and Grams, C.M. (2020) The role of large-scale dynamics in an exceptional sequence of severe thunderstorms in Europe May-June 2018. *Weather and Climate Dynamics*, 1, 325–348.

Molina, M.J., Gagne, D.J. and Prein, A.F. (2021) A benchmark to test generalization capabilities of deep learning methods to classify severe convective storms in a changing climate. *Earth and Space Science*, 8, e2020EA001490.

Nisi, L., Ambrosetti, P. and Clementi, L. (2014) Nowcasting severe convection in the alpine region: the COALITION approach. *Quarterly Journal of the Royal Meteorological Society*, 140, 1684–1699.

Nisi, L., Hering, A., Germann, U. and Martius, O. (2018) A 15-year hail streak climatology for the alpine region. *Quarterly Journal of the Royal Meteorological Society*, 144, 1429–1449.

NOAA SPC. (2014) *Significant Hail Parameter*. Norman, OK: Storm Prediction Center, National Oceanic and Atmospheric Administration. https://www.spc.noaa.gov/exper/mesoanalysis/help/help_sigh.html [Accessed 22nd March 2023].

Orlanski, I. (1975) A rational subdivision of scales for atmospheric processes. *Bulletin of the American Meteorological Society*, 56, 527–530.

Parzen, E. (1962) On estimation of a probability density function and mode. *Annals of Mathematical Statistics*, 33, 1065–1076.

Piper, D. and Kunz, M. (2017) Spatiotemporal variability of lightning activity in Europe and the relation to the North Atlantic oscillation teleconnection pattern. *Natural Hazards and Earth System Sciences*, 17, 1319–1336.

Piper, D., Kunz, M., Ehmele, F., Mohr, S., Mühr, B., Kron, A. and Daniell, J. (2016) Exceptional sequence of severe thunderstorms and related flash floods in May and June 2016 in Germany—part 1: meteorological background. *Natural Hazards and Earth System Sciences*, 16, 2835–2850.

Pison, G., Struyf, A. and Rousseeuw, P.J. (1999) Displaying a clustering with CLUSPLOT. *Computational Statistics and Data Analysis*, 30, 381–392.

1477870x, 2023, 755, Downloaded from https://rmets.onlinelibrary.wiley.com/doi/10.1002/qj.4505 by Karlsruher Institution F. Technologie, Wiley Online Library on [10/11/2023]. See the Terms and Conditions (https://onlinelibrary.wiley.com/terms-and-conditions) on Wiley Online Library for rules of use; OA articles are governed by the applicable Creative Commons License

Prein, A.F. and Holland, G.J. (2018) Global estimates of damaging hail hazard. *Weather and Climate Extremes*, 22, 10–23.

Pscheidt, I., Senf, F., Heinze, R., Deneke, H., Trömel, S. and Hohenegger, C. (2019) How organized is deep convection over Germany? *Quarterly Journal of the Royal Meteorological Society*, 145, 2366–2384.

Púčik, T., Castellano, C., Groenemeijer, P., Kühne, T., Rädler, A.T., Antonescu, B. and Faust, E. (2019) Large hail incidence and its economic and societal impacts across Europe. *Monthly Weather Review*, 147, 3901–3916.

Púčik, T., Groenemeijer, P., Ryva, D. and Kolar, M. (2015) Proximity soundings of severe and nonsevere thunderstorms in Central Europe. *Monthly Weather Review*, 143, 4805–4821.

Rasmussen, E.N. and Blanchard, D.O. (1998) A baseline climatology of sounding-derived supercell and Tornado forecast parameters. *Weather and Forecasting*, 13, 1148–1164.

Rousseeuw, P.J. (1987) Silhouettes: a graphical aid to the interpretation and validation of cluster analysis. *Journal of Computational and Applied Mathematics*, 20, 53–65.

Ryzhkov, A.V., Schuur, T.J., Burgess, D.W., Heinselman, P.L., Giangrande, S.E. and Zrnic, D.S. (2005) The joint polarization experiment: polarimetric rainfall measurements and hydrometeor classification. *Bulletin of the American Meteorological Society*, 86, 809–824.

Saltikoff, E., Haase, G., Delobbe, L., Gaussiat, N., Martet, M., Idziorek, D., Leijnse, H., Novák, P., Lukach, M. and Stephan, K. (2019) OPERA the radar project. *Atmosphere*, 10, 320.

Schmidberger, M. (2018) *Hagelgefährdung und Hagelrisiko in Deutschland basierend auf einer Kombination von Radardaten und Versicherungsdaten (in German only). Wissenschaftliche Berichte des Instituts für Meteorologie und Klimaforschung des Karlsruher Instituts für Technologie (KIT)*, Vol. 78. Karlsruhe: KIT Scientific Publishing. https://doi.org/10.5445/KSP/1000086012.

Schraff, C. (1996) *Data assimilation and mesoscale weather prediction: a study with a forecast model for the alpine region*. Scientific Report. Veröffentlichungen der Schweizerischen Meteorologischen Anstalt, Swiss Meteorological Institute, Zurich. https://www.meteoswiss.admin.ch/dam/jcr:9b98399a-69e6-4205-acdf-941c26fc367b/veroeff56.pdf [Accessed 22nd March 2023].

Schraff, C. (1997) Mesoscale data assimilation and prediction of low stratus in the alpine region. *Meteorology and Atmospheric Physics*, 64, 21–50.

Schraff, C. and Hess, R. (2013) *A Description of the Nonhydrostatic Regional COSMO-Model—Part III: Data Assimilation. Consortium for Small-Scale Modelling*. Offenbach: Deutscher Wetterdienst. http://www.cosmo-model.org/content/model/cosmo/coreDocumentation/cosmo_assimilation_5.00.pdf [Accessed 22nd March 2023].

Schulz, J.-P. and Schättler, U. (2014) *Kurze Beschreibung des Lokal-Modells Europa COSMO-EU (LME) und seiner Datenbanken auf dem Datenserver des DWD (in German only)*. Offenbach: Deutscher Wetterdienst. https://www.dwd.de/SharedDocs/downloads/DE/modelldokumentationen/nwv/cosmo_eu/cosmo_eu_dbbeschr_201406.pdf?__blob=publicationFile&v=3 [Accessed 22nd March 2023].

Sherburn, K.D. and Parker, M.D. (2014) Climatology and ingredients of significant severe convection in high-shear, low-CAPE environments. *Weather and Forecasting*, 29, 854–877.

Sherburn, K.D., Parker, M.D., King, J.R. and Lackmann, G.M. (2016) Composite environments of severe and nonsevere high-shear, low-CAPE convective events. *Weather and Forecasting*, 31, 1899–1927.

Stephan, K., Klink, S. and Schraff, C. (2008) Assimilation of radar-derived rain rates into the convective-scale model COSMO-DE at DWD. *Quarterly Journal of the Royal Meteorological Society*, 134, 1315–1326.

Tang, B.H., Gensini, V.A. and Homeyer, C.R. (2019) Trends in United States large hail environments and observations. *npj Climate and Atmospheric Science*, 2, 45.

Taszarek, M., Allen, J., Púčik, T., Groenemeijer, P., Czernecki, B., Kolendowicz, L., Lagouvardos, K., Kotroni, V. and Schulz, W. (2019) A climatology of thunderstorms across Europe from a synthesis of multiple data sources. *Journal of Climate*, 32, 1813–1837.

Taszarek, M., Allen, J.T., Púčik, T., Hoogewind, K.A. and Brooks, H.E. (2020) Severe convective storms across Europe and the United States. Part II: ERA5 environments associated with lightning, large hail, severe wind, and tornadoes. *Journal of Climate*, 33, 10263–10286.

Taszarek, M., Pilguj, N., Allen, J., Gensini, V., Brooks, H. and Szuster, P. (2021) Comparison of convective parameters derived from ERA5 and MERRA2 with rawinsonde data over Europe and North America. *Journal of Climate*, 34, 3211–3237.

Thompson, R.L., Edwards, R., Hart, J.A., Elmore, K.L. and Markowski, P. (2003) Close proximity soundings within supercell environments obtained from the rapid update cycle. *Weather and Forecasting*, 18, 1243–1261.

Trapp, R.J. (2013) *Mesoscale-Convective Processes in the Atmosphere*. Cambridge: Cambridge University Press.

Ukkonen, P. and Mäkelä, A. (2019) Evaluation of machine learning classifiers for predicting deep convection. *Journal of Advances in Modeling Earth Systems*, 11, 1784–1802.

Ukkonen, P., Manzato, A. and Mäkelä, A. (2017) Evaluation of thunderstorm predictors for Finland using reanalyses and neural networks. *Journal of Applied Meteorology and Climatology*, 56, 2335–2352.

Van der Laan, M., Pollard, K. and Bryan, J. (2003) A new partitioning around medoids algorithm. *Journal of Statistical Computation and Simulation*, 73, 575–584.

Vogel, K., Ozturk, U., Riemer, A., Laudan, J., Sieg, T., Wendi, D., Agarwal, A., Rözer, V., Korup, O. and Thieken, A. (2017) Die Sturzflut von Braunsbach am 29. Mai 2016 - Entstehung, Ablauf und Schäden eines "Jahrhundertereignisses". Teil 2: Geomorphologische Prozesse und Schadensanalyse (in German only). *Hydrologie und Wasserbewirtschaftung*, 61, 163–175.

Wang, Y., Coning, E.D., Harou, A., Jacobs, W., Joe, P., Nitina, L., Roberts, R., Wang, J., Wison, J., Atenica, A., Bica, B., Brown, B., Goodmann, S., Kann, A., Li, P.W., Monteiro, I., Parrish, P., Schmid, F., Seed, A. and Sun, J. (2017) *Guidelines for Nowcasting Techniques*. Geneva: World Meteorological Organization. https://library.wmo.int/doc_num.php?explnum_id=3795 [Accessed 22nd March 2023].

Wapler, K. (2017) The life-cycle of hailstorms: lightning, radar reflectivity and rotation characteristics. *Atmospheric Research*, 193, 60–72.

Wapler, K. (2021) Mesocyclonic and non-mesocyclonic convective storms in Germany: storm characteristics and life-cycle. *Atmospheric Research*, 248, 105186.

Wapler, K., Bañón Peregrn, L.M., Buzzi, M., Heizenreder, D., Kann, A., Meirold-Mautner, I., Simon, A. and Wang, Y.

1477870x, 2023, 755, Downloaded from https://rmets.onlinelibrary.wiley.com/doi/10.1002/qj.4505 by Karlsruher Institution F. Technologie, Wiley Online Library on [10/11/2023]. See the Terms and Conditions (https://onlinelibrary.wiley.com/terms-and-conditions) on Wiley Online Library for rules of use; OA articles are governed by the applicable Creative Commons License

(2018) Conference report 2nd European nowcasting conference. *Meteorologische Zeitschrift*, 27, 81–84.

Wapler, K. and James, P. (2015) Thunderstorm occurrence and characteristics in Central Europe under different synoptic conditions. *Atmospheric Research*, 158-159, 231–244.

Weisman, M.L. and Klemp, J.B. (1982) The dependence of numerically simulated convective storms on vertical wind shear and buoyancy. *Monthly Weather Review*, 110, 504–520.

Werner, M. (2020) Kurzbeschreibung KONRAD3D, version 1.3.2. Deutscher Wetterdienst, Offenbach. (Personal communication).

Westermayer, A., Groenemeijer, P., Pistotnik, G., Sausen, R. and Faust, E. (2017) Identification of favorable environments for thunderstorms in reanalysis data. *Meteorologische Zeitschrift*, 26, 59–70.

Weusthoff, T. and Hauf, T. (2008) Basic characteristics of post-frontal shower precipitation rates. *Meteorologische Zeitschrift*, 17, 793–805.

Wilhelm, J. (2022) *Einfluss atmosphärischer Umgebungsbedingungen auf den Lebenszyklus konvektiver Zellen in der Echtzeit-Vorhersage (in German only). Wissenschaftliche Berichte des Instituts für Meteorologie und Klimaforschung des Karlsruher Instituts für Technologie (KIT)*, Vol. 85. Karlsruhe: KIT Scientific Publishing. https://doi.org/10.5445/KSP/1000145542.

Wilhelm, J., Mohr, S., Punge, H.J., Mühr, B., Schmidberger, M., Daniell, J.E., Bedka, K.M. and Kunz, M. (2021) Severe thunderstorms with large hail across Germany in June 2019. *Weather*, 76, 228–237.

Wilks, D.S. (2006) *Statistical Methods in the Atmospheric Sciences*, 2nd edition. San Diego, CA: Academic Press.

Zöbisch, I., Forster, C., Zinner, T., Bugliaro, L., Tafferner, A. and Wapler, K. (2020) Characteristics of deep moist convection over Germany in multi-source data. *Meteorologische Zeitschrift*, 29, 393–407.

SUPPORTING INFORMATION

Additional supporting information can be found online in the Supporting Information section at the end of this article.

How to cite this article: Wilhelm, J., Wapler, K., Blahak, U., Potthast, R. & Kunz, M. (2023) Statistical relevance of meteorological ambient conditions and cell attributes for nowcasting the life cycle of convective storms. *Quarterly Journal of the Royal Meteorological Society*, 149(755), 2252–2280. Available from: https://doi.org/10.1002/qj.4505

APPENDIX A

A.1 Life-cycle properties: Parabola model

As reported by Wapler (2021), a mean parabolic evolution of the cell area A for isolated convection, and a high variability between life cycles is apparent (Figure A1a,b). Based on multiyear KONRAD statistics and case studies of several prominent storms, the DWD implemented a parametric parabola life-cycle model for cell area evolution in combination with an ensemble Kalman filter into the successor KONRAD3D (Feger *et al.*, 2019; Werner, 2020). The parabolic curves for short lifetimes in Figure A1a,b are smoother than those for long lifetimes, as they are based on a larger number of single-cell life cycles. Especially during the first 15 min after the first detection of the cells, the mean growth rates of long-living cells appear to be higher than those of short-living cells with a lifetime below approximately 60 min. However, within a wide range of long-living cells, growth rates are rather comparable. The respective variation ranges strongly overlap, even with the ranges of short-living cells.

As a proxy for convection intensity, the ratio of cell core area A_C ($Z \geq 55$ dBZ) and entire cell area A ($Z \geq 46$ dBZ) indicates the high-reflectivity fraction of a cell (Figure A1c,d). The mean ratio grows faster for long-living than for short-living cells. This finding, which supports the hints of Davini *et al.* (2012), underpins that initial rapid and intense cell growth (i.e., a rapid increase in both the cell area and the core area) can be a good indication of a long lifetime. The reason for this could be a previous rapid intensification of the cell's updraught, which promotes both vertical growth and horizontal extension of the deep convection cell. This may lead to precipitation formation in a large air volume, which is reflected in high reflectivity values shortly thereafter. Such a rapid cell development was observed, for example, for the supercell of July 28, 2013 (Kunz *et al.*, 2018).

Similar to the approach of Weusthoff and Hauf (2008), the parabola family of cell area can be described by

$$A^{(T)}(t) = A^{(T)}_{\max} - \frac{A^{(T)}_{\max} - A^{(T)}_{\min}}{(T/2)^2}\left(t - \frac{T}{2}\right)^2. \qquad \text{(A1)}$$

Here, A again represents the mean cell area, T the lifetime (form parameter), and t cell age. The difference $A^{(T)}_{\max} - A^{(T)}_{\min}$ can be called the maximum evolution amplitude $\mathcal{A}$ of the mean cell areas. As can be estimated from Figure A1a, mean maximum amplitude $\mathcal{A}$ and lifetime T are linearly highly correlated ($r_{\text{Pearson}} = 0.74$, $r_S = 0.73$) so that $\mathcal{A}^{(T)} \approx c_A T$. Linear regression without intercept yields $c_A = 0.295\,\text{km}^2\cdot\text{min}^{-1}$, with an RMSE of the amplitude of $4.2\,\text{km}^2$. The minimum of cell area $A^{(T)}_{\min}$ is assumed to be taken at the first cell detection, showing similar values for the entire cell spectrum. Thus, a constant fit leads to $A^{(T)}_{\min} \approx A_0 = 21.3 \pm 1.1\,\text{km}^2$ (RMSE). Hence, Equation (A1) may be rewritten as

$$A^{(T)}(t) = A_0 + 4c_A t\left(1 - \frac{t}{T}\right), \qquad \text{(A2)}$$

1477870x, 2023, 755, Downloaded from https://rmets.onlinelibrary.wiley.com/doi/10.1002/qj.4505 by Karlsruher Institution F. Technologie, Wiley Online Library on [10/11/2023]. See the Terms and Conditions (https://onlinelibrary.wiley.com/terms-and-conditions) on Wiley Online Library for rules of use; OA articles are governed by the applicable Creative Commons License

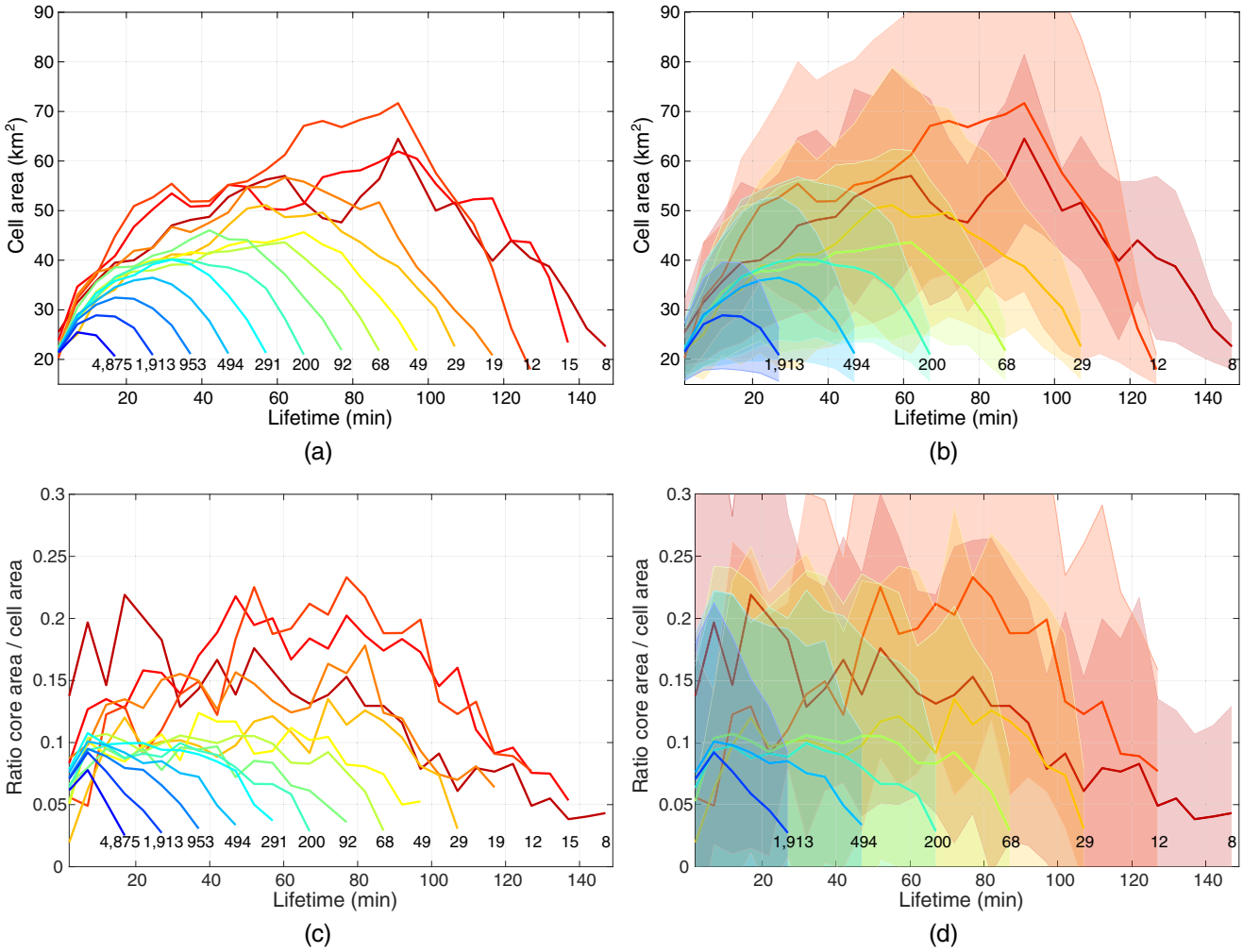


FIGURE A1 Mean time evolution of (a) cell area A and (c) the ratio of cell core area and cell area A_C/A, sorted by cell lifetime. Different line colours indicate different lifetimes. The numbers at the line ends indicate the number of cells that contributed to the averaging. For the sake of clarity, only every second line of the 5-min cell statistics is drawn. (b, d) Like (a) and (c), except that only every fourth line is drawn, but with a variation range corresponding to the standard deviation (1σ interval). [Colour figure can be viewed at wileyonlinelibrary.com]

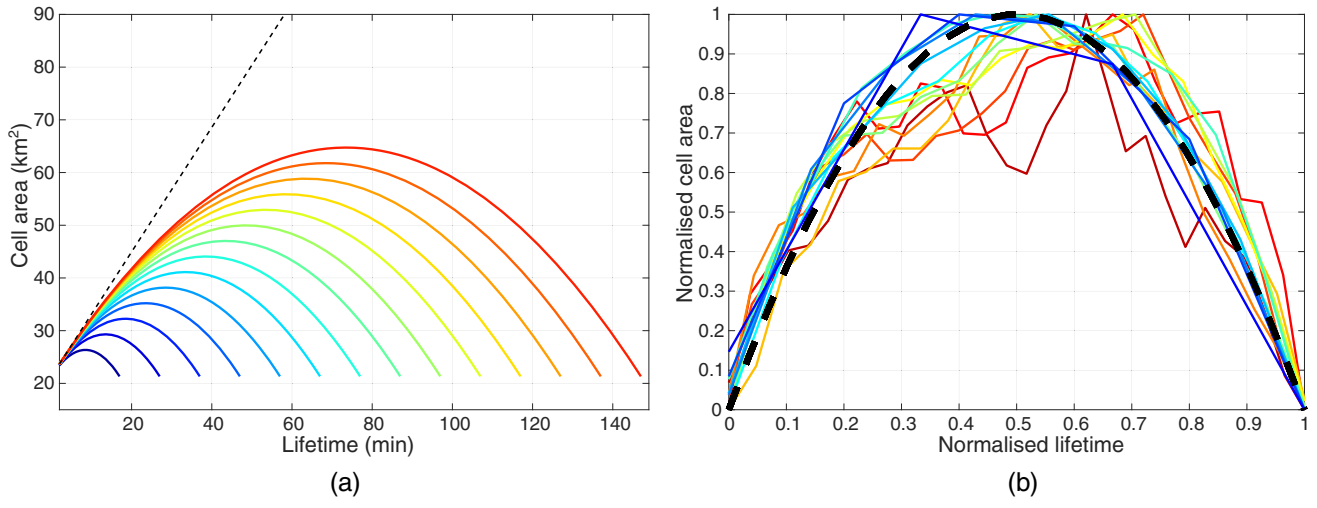


FIGURE A2 (a) Parabola family of the analytical model according to Equation (A2) for the temporal evolution of the mean cell area $A(t)$ with lifetime T as form parameter. The limitation of the range of values is indicated by the black dashed line. (b) Mean evolution of the normalised cell area with respect to the corresponding life cycle. The black dashed line is the curve of the normalised parabolic model. As in Figure A1a, only every second line of the 5-min cell statistics is drawn. [Colour figure can be viewed at wileyonlinelibrary.com]

1477870x, 2023, 755, Downloaded from https://rmets.onlinelibrary.wiley.com/doi/10.1002/qj.4505 by Karlsruher Institution F. Technologie, Wiley Online Library on [10/11/2023]. See the Terms and Conditions (https://onlinelibrary.wiley.com/terms-and-conditions) on Wiley Online Library for rules of use; OA articles are governed by the applicable Creative Commons License

limiting the values of the parabola family to $A_{crit}(t) = A_0 + 4c_A t$ (black dashed line in Figure A2a).

Normalising the cell amplitudes $A^{(T)}(t) - A_0$ by the maximum amplitude $\mathcal{A}$ and the time t by the cells' lifetime T reduces the parabola family to one single representative parabola describing the mean amplitude-normalised cell area evolution during a normalised life cycle (black dashed line in Figure A2b). As can be seen from the observations in Figure A2b, and as Davini *et al.* (2012) reported for cells in northern Italy, with increasing (absolute) lifetime, the (relative) time when the maximum cell area is reached is shifted to later life-cycle stages, an asymmetry, which is not reflected in the parabola model. One possible explanation could be that cells with a particularly intense and broad updraught, and thus a large vertical extent, achieve a long lifetime, as they increasingly expand horizontally during the life cycle. These cells possibly reach the largest cell area after the time of the highest maximum storm intensity (in terms of high reflectivity area). The somewhat faster relative decrease in the cell area towards the end of the life cycle could be attributed to a widespread weakening of precipitation formation in regions far from the residual cell core, which would lead to a reflectivity decrease to values below KONRAD's minimum detection criterion of $Z = 46$ dBZ there. In conclusion, an axially symmetric parabola describes the mean cell area evolution well but with second-order limitations concerning the timing of the maximum cell area during the life cycle.

A.2 Additional table and figures

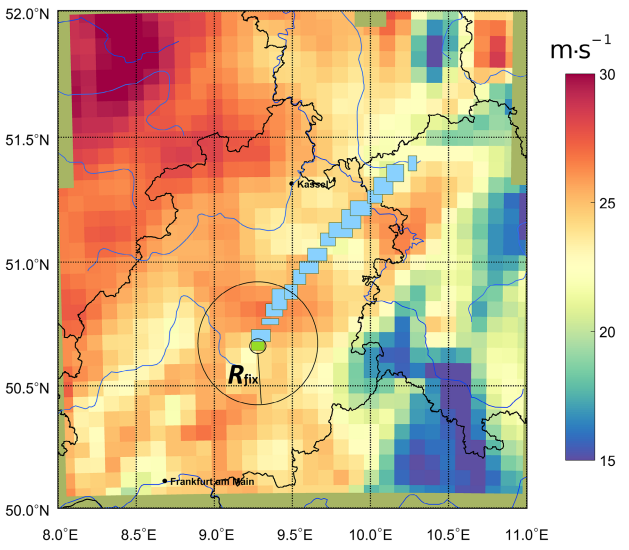


FIGURE A3 Combined illustration of deep-layer shear (m·s^{-1}), as calculated from COSMO-EU assimilation analyses, and the KONRAD track of a long-living thunderstorm cell in central Germany on September 11, 2011 (1500 UTC). The KONRAD cell is depicted for all following 5-min detections by light blue rectangles, which enframe all radar pixels belonging to the respective detection. For the first cell detection at 1500 UTC (green rectangle), the cell surrounding is drawn as the outer black circle, obtained by first drawing the inner circle enclosing the rectangle minimally and then adding the fixed radius R_{fix}. [Colour figure can be viewed at wileyonlinelibrary.com]

1477870x, 2023, 755, Downloaded from https://rmets.onlinelibrary.wiley.com/doi/10.1002/qj.4505 by Karlsruher Institution F. Technologie, Wiley Online Library on [10/11/2023]. See the Terms and Conditions (https://onlinelibrary.wiley.com/terms-and-conditions) on Wiley Online Library for rules of use; OA articles are governed by the applicable Creative Commons License

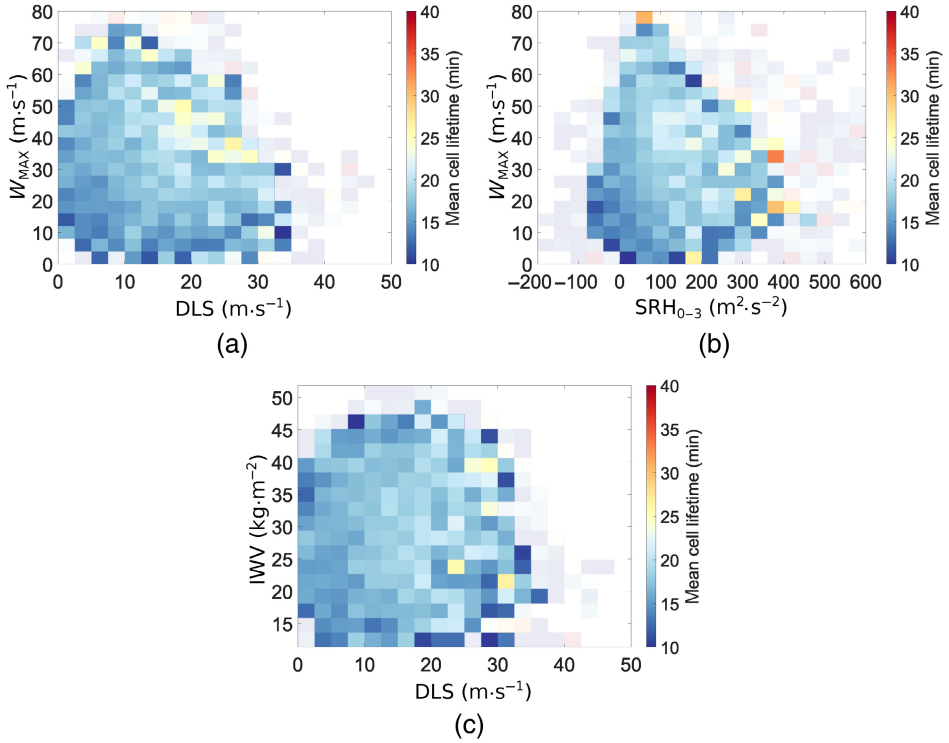


FIGURE A4 Like Figure 13c but depending on (a) deep-layer shear (DLS) and maximum updraught velocity W_{MAX}, (b) SRH_{0-3} and W_{MAX}, and (c) DLS and vertically integrated water vapour (IWV). [Colour figure can be viewed at wileyonlinelibrary.com]

TABLE A1 Summary of the abbreviations used for the relevant ambient variables in the main text and in figures and their respective descriptions.

Abbreviation	Description
BRN_{MU}	MU bulk Richardson number
$CAPE_{MU}$	MU convective available potential energy
CIN_{MU}	MU convective inhibition
DCI_{ML}	ML deep convective index
DLS	Deep-layer shear (0–6 km AGL)
$\Delta\theta_e$	$\theta_{e,sfc} - \theta_{e,300}$
EL_{MU}	MU equilibrium level
$h_{0°C}$	0°C-level height
IWV	Vertically integrated water vapour content
KO index	KO index
LCL_{MU}	MU lifting condensation level
LFC_{MU}	MU level of free convection
LI_{ML}	ML lifted index
$LR_{700-500}$	Mean lapse rate between 700 and 500 hPa
MLS	Medium-layer shear (0–3 km AGL)
RH_{700}	700 hPa relative humidity
SCP	Supercell composite parameter
SHIP	Significant hail parameter
SI	Showalter index
SRH_{0-1}	0–1 km storm relative helicity
$SRH_{0-1.5}$	0–1.5 km storm relative helicity
SRH_{0-3}	0–3 km storm relative helicity
$T_{2\,m}$	2 m temperature
T_{850}	850 hPa temperature
$\theta_{e,850}$	850 hPa pseudoequivalent potential temperature
U_{0-3}	Mean horizontal wind (0–3 km AGL)
U_{0-6}	Mean horizontal wind (0–6 km AGL)
U_{0-10}	Mean horizontal wind (0–10 km AGL)
U_{3-6}	Mean horizontal wind (3–6 km AGL)
VT	Vertical totals index
Z_{500}	500 hPa geopotential

Note: For T_{850} and $\theta_{e,850}$, the standard deviation in the cell surroundings is considered as a separate variable in addition (see Section 2.3), resulting in 33 ambient variables in total.
Abbreviations: AGL, above ground level; ML, mixed layer; MU, most unstable.

1477870x, 2023, 755, Downloaded from https://rmets.onlinelibrary.wiley.com/doi/10.1002/qj.4505 by Karlsruher Institution F. Technologie, Wiley Online Library on [10/11/2023]. See the Terms and Conditions (https://onlinelibrary.wiley.com/terms-and-conditions) on Wiley Online Library for rules of use; OA articles are governed by the applicable Creative Commons License